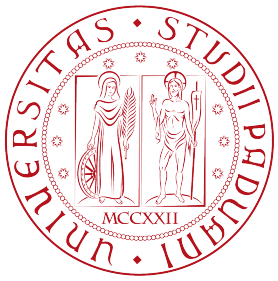

UNIVERSITÀ DEGLI STUDI DI PADOVA

SCUOLA DI SCIENZE

Dipartimento di Geoscienze
Direttore Prof.ssa Cristina Stefani

TESI DI LAUREA MAGISTRALE
IN
GEOLOGIA E GEOLOGIA TECNICA

THERMOELASTIC PARAMETERS OF COESITE: IMPLICATIONS FOR DIAMOND GEOBAROMETRY

Relatore: Prof. Fabrizio Nestola
Correlatori: Dott. Matteo Alvaro
Dott. Donato Belmonte
Dott. Mauro Prencipe

Laureanda: Chiara Anzolini

ANNO ACCADEMICO 2013/ 2014

Abstract

Coesite is one of the most studied phases in high-pressure mineralogy and petrology as it represents a real high-pressure marker characterized by an extremely simplified chemistry. For this reason, since its discover several scientists tried to use coesite as a geobarometer with the final aim to provide an exact value of crystallization pressure. However, nobody was really able to obtain such information from coesite so far. Considering that this would provide an estimate of pressure of formation for coesite-bearing eclogitic rocks, the use of coesite as a geobarometer could be of extreme help.

This master thesis will be focused on the geobarometry of diamond relatively to the coesite-diamond pair starting from the pioneering work published in 2000 by Sobolev et al. on PNAS magazine. In that work the authors applied the so-called “elastic method” to obtain the residual pressure and then to calculate the pressure of formation of diamond and coesite.

However, it is today accepted that some thermoelastic parameters of coesite (i.e. thermal expansion and dependence of bulk modulus with temperature) do not allow to obtain reliable values of pressure of formation for the coesite-diamond pair.

In this thesis work I have obtained new thermal expansion data on coesite beyond the dependency of the bulk modulus with temperature. This last parameter was measured by using Resonant Ultrasound Spectroscopy at low temperature, whereas the thermal expansion was determined by first-principles methods.

My results indicate both that the coesite-diamond pair cannot be considered a reliable geobarometer yet, and that the improved “elastic method”, together with the isomeke calculation, need a more-in-depth study on its range of use. In addition, it was demonstrated that the pioneering work by Sobolev et al. (2000) reported wrong calculations on the pressure of formation of coesite.

Riassunto

La coesite è una delle fasi più studiate nell'ambito della mineralogia di alta pressione poiché si tratta di un vero e proprio *marker* di alta pressione caratterizzato da una chimica estremamente semplificata. Per questo motivo, fin dalla sua scoperta numerosi studiosi hanno tentato di utilizzarla come geobarometro allo scopo di ricavarne un valore esatto di pressione di cristallizzazione. Finora, tuttavia, nessuno è stato in grado di raggiungere tale scopo. Considerando che questo dato fornirebbe anche una stima della pressione di formazione per le rocce eclogitiche a coesite, l'uso di questo minerale come geobarometro potrebbe essere di grande utilità.

Questa tesi si focalizzerà sulla geobarometria del diamante relativamente alla coppia diamante-coesite, partendo dal lavoro pionieristico di Sobolev et al. pubblicato nel 2000 su PNAS. In quel lavoro gli autori applicarono il cosiddetto "metodo elastico" per ottenere la pressione residua dell'inclusione e, di conseguenza, la pressione di formazione sia del diamante che della coesite.

Oggi, tuttavia, è comunemente accettato che alcuni parametrici termoelastici della coesite (ad es. l'espansione termica e la dipendenza del *bulk modulus* con la temperatura) non consentano di ottenere valori affidabili di pressione di formazione per la coppia diamante-coesite.

In questo lavoro di tesi ho ottenuto nuovi dati sull'espansione termica della coesite, oltre alla dipendenza del *bulk modulus* con la temperatura. Quest'ultimo parametro è stato misurato utilizzando la *Resonant Ultrasound Spectroscopy* a bassa temperatura, mentre l'espansione termica è stata determinata con metodi *ab initio.*

I miei risultati indicano sia che la coppia diamante-coesite non può ancora essere considerata un geobarometro affidabile, sia che il "metodo elastico" aggiornato con il calcolo delle isomeke necessita di uno studio più approfondito sul suo range di efficacia. Inoltre, è stato dimostrato che il lavoro pionieristico di Sobolev et al. (2000) riportava calcoli errati sulla pressione di formazione della coesite.

Contents

1. Introduction 1
1.1. Classical geothermobarometric methods versus the "elastic method" 2
2. History of coesite 6
3. What is coesite? 8
4. Method for determining the pressure of formation of diamond-inclusion pairs 10
4.1. The concept of "isomeke" 10
4.2. The role of elastic relaxation 12
5. Piston-cylinder apparatus 14
5.1. Introduction 14
5.2. History 14
5.3. Theory 15
5.4. Components 15
5.4.1. Sample assemblies 17
5.4.2. Capsules 18
5.5. Pressure control 19
5.6. Temperature control 19
6. Synthesis of material 20
6.1. Synthesis of coesite in single crystal 20
6.2. Polycrystalline samples 21
7. Samples characterization 30
7.1. Single crystals 30
7.1.1. MicroRaman spectroscopy 30
7.1.2. Single-crystal X-ray diffraction 31
7.2. Polycrystalline samples 32
8. Resonant Ultrasound Spectroscopy 39
8.1. Introduction 39
8.2. History 39
8.3. Overview 40
8.4. RUS apparatus 42
8.4.1. Room-temperature apparatus 43
8.4.2. Low-temperature apparatus 44
8.4.3. Samples 44
8.4.4. Transducers 45
9. RUS data collection 47
9.1. Sample description 47
9.2. Room-temperature RUS experiments 47
9.3. Low-temperature RUS experiments 48
9.4. Data analysis 49
9.4.1. Frequency and Q^{-1} analysis 49

10. RUS results **52**
10.1. Room-temperature results **52**
10.2. Low-temperature results **53**
10.3. Elastic moduli **56**
11. First principles methods **58**
11.1. Introduction **58**
11.2. The *ab initio* approaches **59**
11.2.1. The Hartree-Fock method 60
11.2.2. The Density Functional Theory 60
12. Coesite thermal expansion data **61**
13. Thermal expansion **63**
13.1. Background **63**
13.2. *P-V-T* equations of state **65**
14. Pressure of formation: EosFit software as a main calculation tool **66**
15. Conclusions **72**
References **75**
Acknowledgments **81**
A. Equations of State **83**
B. Mathematical theory behind RUS **86**
B.I. Lagrangian minimization **86**
B.II. Rayleigh-Ritz Variational Method **88**
B.III. The Inverse Problem **88**
C. Text for the "lorentz2" peak fitting function **89**
D. Calculation to infer the G from the K_S **90**

1. Introduction

The knowledge of pressure and temperature conditions at which geological processes occur plays a key role in Earth Sciences as this provides crucial information about the evolution with time of our Planet.

In detail, geologists call "geobarometry" and "geothermometry" (or in general "geothermobarometry" combining the two terms) those tools used in geology to indicate the approaches to determine the pressure (*P*) and the temperature (*T*) of formation, respectively, of a mineral and/or a rock. Even more intriguing is the application of geothermobarometry when the target of the scientific investigation is the Earth's mantle. This is mainly due to the fact that mantle can extend to about 2900 km depth at the boundary with the outer core. The only direct and unaltered samples that can reach the surface of Earth from such depths are diamonds. When diamonds carry mineral inclusions to the surface, then we have real "deep Earth fragments" which can provide unique information on "what" there is and "what happens" at great depths inside our Planet. About 94% of diamonds grow in the upper mantle, in the so-called "diamond window" (Fig. 1.1; Stachel and Harris, 2008), whereas only 6% of them are considered of very deep origin (known as "super-deep diamonds"). It is very well known that the upper mantle, extending from the boundary with the Earth's crust to about 410 km, is the main responsible for plate tectonics and several crucial geological processes, therefore the study of mineral inclusions still trapped in diamonds becomes the only possibility to sample very deep material.

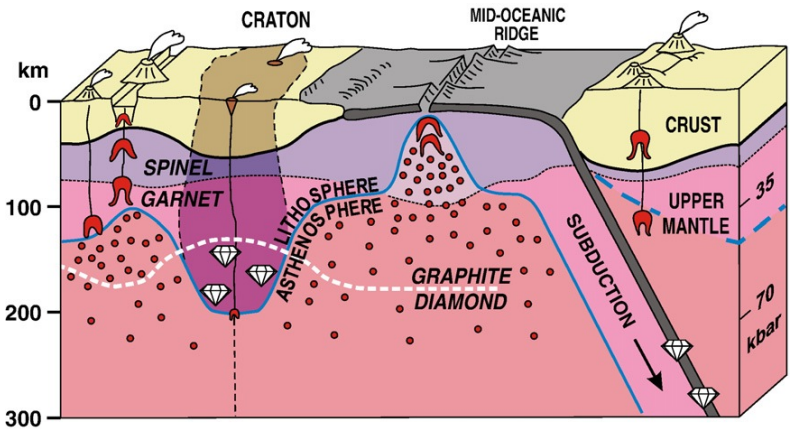

Fig. 1.1: Schematic vertical section through the Earth's crust and part of the upper mantle (from Stachel and Harris, 2008).

Mantle geologists focused since several years on understanding at which pressure and temperature rocks and minerals form and in order to obtain such information they developed different methods based on the chemistry and on the cation partitioning in minerals. At the same time mineral physicists developed an alternative geothermobarometric method, which instead is based on thermoelastic parameters of the minerals under investigation.

Here below I will provide an overview of the two completely different approaches reviewing advantages and disadvantages of both in light of my master thesis concerning coesite.

1.1. Classical geothermobarometric methods versus the "elastic method"

Classical geothermobarometry allows one to retrieve the temperature and the pressure of formation of a mineral species or a mineral assemblage knowing the chemical compositions of the minerals and how these compositions vary with *P* and/or *T* of formation. Basically, normal thermobarometers rely on chemical equilibria between at least two minerals. However, the difficulty to find suitable mineral couples has made it necessary to devise some formulations based on one single mineral. These formulations assume the composition of this mineral being in equilibrium with another phase capable of buffering its composition under certain *P* and *T*. Such single-mineral thermobarometers, despite of their assumptions, are very useful in particular for diamond studies because: (*i*) most inclusions in diamonds are made of isolated minerals; (*ii*) not-touching inclusions in the same diamond may have been trapped at different times and *P*-*T* conditions and thus may not have been in equilibrium; (*iii*) touching inclusions presumably had enough time to re-equilibrate at depth after diamond formation during long-standing permanence in the mantle. Single-mineral thermobarometry of monomineralic inclusions will provide an indication of the *P*-*T* of formation of the diamond, provided the inclusions are syngenetic, or had time to re-equilibrate completely during the growth of diamond, and did not undergo any transformation afterwards. Conversely, two-mineral thermobarometry of touching

inclusions may not necessarily provide the temperature of diamond formation, although the pressure estimate will still provide an indication of the depth of provenance of the diamond.

In view of the above considerations, single-mineral thermobarometry on monomineralic inclusions is thought to be the one of the best instruments to measure the true *P*-*T* conditions of diamond formation. However, considering the wide range of pressures and temperatures under which diamonds may form, the potentially large influence of input *P* on *T* estimates, and the possible formation of diamond under perturbed or ancient thermal conditions, the most useful mineral species will be those that demonstrably allow sufficiently accurate retrieval of both *P* and *T* of formation, like diopsides and majorite-rich garnets.

To summarize, to apply such methods strong assumptions have to be taken and the results are often not so precise. Moreover, "chemical methods" can be applied for diamond geobarometry only in 1% of the cases where inclusions are found in diamond: what about the other ~99% of the diamond-inclusion pairs on which classical geothermobarometry cannot be applied?

As already mentioned above, in the last few years a new method, the so-called "elastic method", has been used to determine the pressure and temperature of formation of the diamond-inclusion pairs. Elastic methods provide a potential, generally non-destructive alternative to chemical thermobarometry for the evaluation of the pressure of formation of a diamond containing a monomineralic inclusion. These methods are based on the measurement of the "internal pressure" (P_i, also called "residual" or "remnant" pressure), that is the pressure exerted by the diamond on the inclusion at ambient conditions. Such pressure can be retrieved by using three different techniques: (1) microRaman spectroscopy (e.g., Izraeli et al., 1999; Sobolev et al., 2000; Nasdala et al., 2003; Barron et al., 2008); (2) strain birefringence analysis (Howell et al., 2010), and (3) single-crystal X-ray diffraction (Nestola et al., 2012). Combining the *Pi* with thermoelastic parameters (i.e. volume bulk modulus and its pressure and temperature derivatives, volume thermal expansion, shear modulus) of the diamond and of the inclusion allows one

to calculate an *isomeke* (see Chapter 4), i.e., a curve in *P*-*T* space along which the volume of the inclusion is equal to the volume of the cavity within the diamond for a fixed value of P_i. Such line constrains the possible conditions under which the diamond and the inclusion formed. If *T* is known independently or the isomeke is not strongly dependent on *T*, then the *P* at the time of entrapment of the inclusion can be determined.

Available estimates of the pressure of formation for coesite inclusions based on P_i data are generally much too low for diamond stability (Fig. 1.2). On the whole, *P* estimates for olivine are more acceptable, but they still straddle the graphite-diamond boundary, indicating again some *P* underestimation at least for some samples (Fig. 1.2). The limited success of elastic methods so far indicates that either the diamonds do not have a purely elastic behaviour or that thermoelastic data for the minerals are inaccurate (see the recent review by Howell et al., 2012). The potential applicability of elastic methods to inclusions of important minerals for which single-mineral chemical barometers cannot be employes (e.g., coesite, olivine, chromite) makes these methods worthy of further testing. However, re-assessment of thermoelastic parameters for the minerals included in diamond using state-of-the-art techniques and equipment is necessary before these methods can be considered trustworthy.

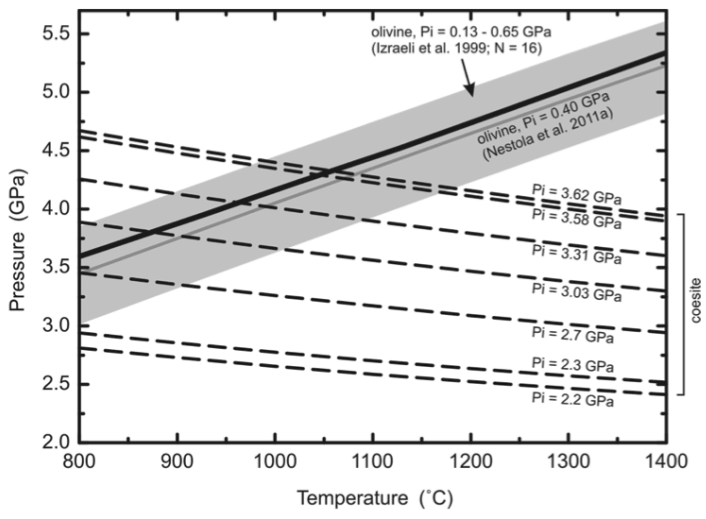

Fig. 1.2: Isomekes for inclusions in diamonds based on P_i estimates (see text for details) obtained using different techniques and thermoelastic parameters as in Howell et al. (2010). Sources of P_i data: olivine - Izraeli et al. (1999; Raman, grey band), Nestola et al. (2011; X-ray diffraction, grey line); coesite - Sobolev et al. (2000; Raman), Nasdala et al. (2003; Raman), Barron et al. (2008; Raman), Howell et al. (2010; birefringence analysis). Black solid line: graphite-diamond boundary after Day (2012).

With the aim to pursue this goal, I will try to measure or to calculate new and more accurate thermoelastic parameters of coesite and I will adopt the “elastic method” in order to retrieve geobarometric information on eclogitic diamonds from different diamond mines all over the world. Indeed, coesite could be the perfect candidate for eclogite geobarometry as such mineral shows an extremely simplified chemistry and is often found in diamonds perfectly preserved as single crystal being one of the most important high-pressure markers in geology.

2. History of coesite

Coesite, a high-pressure polymorph of silica (SiO_2), was first synthesized and described by Coes (1953). The first natural occurrence was reported by Chao et al. (1960) from Meteor Crater, Arizona, and many similar occurrences have then been reported from other impact structures.

The first alleged coesite-bearing metamorphic rocks were reported by two Russian geologists (Chesnokov and Popov, 1965). They described inclusions of quartz aggregate in eclogitic garnets from the south Ural Mountains. Radiating fractures that were believed to be caused by the volume increase in transformation from coesite to quartz surrounded these quartz inclusions. This occurrence, unfortunately, has never been confirmed and was not publicized perhaps because the paper was published in Russian.

Three years later, the first identification by X-ray studies of coesite in a diamond (Harris, 1968) gave way to a consideration about a possible key role of this mineral in the upper mantle. In the next decade several discovers followed one another validating the hypothesis of a possible eclogite paragenesis of coesite in natural diamonds. First a full eclogitic assemblage constituted by garnet, omphacite and coesite was found as mineral inclusions in two diamond crystals from placers of the northeastern Siberian Platform (Sobolev et al., 1976). Then, other findings of xenoliths of coesite eclogites in the Roberts Victor kimberlite pipe, RSA (Smyth and Hatton, 1977), and Udachnaya pipe, Yakutia (Ponomarenko et al., 1977), confirmed the validity of this theory.

At that time, however, coesite was thought to be formed only in the Earth's mantle, on the Earth's surface as product of meteoritic impacts, and in some meteorites.

It was not until the middle of 1980s that coesite was first discovered as inclusions in pyropes from quartzites in the Dora Maira area of the Western Alps of Italy by Chopin (1984) (Fig. 2.1), and independently, almost at the same time, it was also discovered as inclusions in clinopyroxene from eclogites in the Western Gneiss Region of Norway by Smith (1984). These discoveries were the

first to demonstrate clearly that there are some crustal rocks that have been metamorphosed at pressures greater than 2.8 GPa at a temperature of 700°C.

The above revolutionary discovers arouse an extremely high interest to search for relict coesite in metamorphic rocks as only these relics can be considered the most convincing proof of UHP metamorphism.

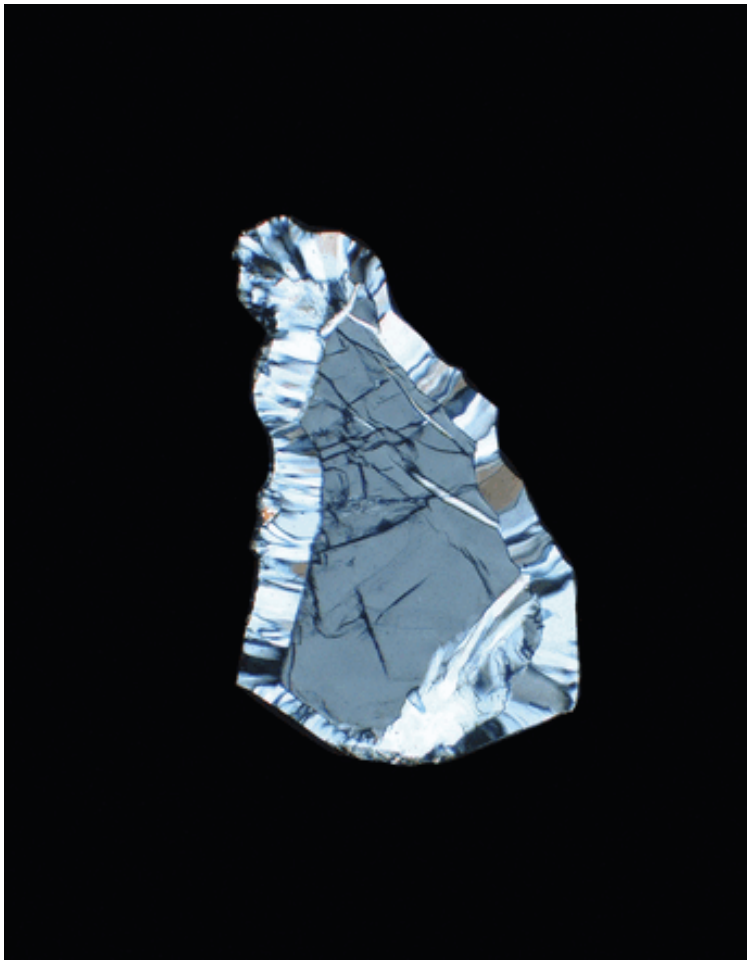

Fig. 2.1: An inclusion of coesite surrounded by a striped rim of palisade quartz and trapped in garnet (black) is a classic indicator of ultrahigh-pressure metamorphism. The quartz forms from the incomplete transformation of coesite during decompression. From a pyrope quartzite, Dora-Maira massif, Italy. The inclusion is approximately 100 μm long and is shown under crossed polarizers. Photo courtesy of Hans-Peter Schertl (from Elements, 2013).

3. What is coesite?

Coesite is a high-pressure polymorph of silica (SiO_2), which forms when quartz undergoes pressures of 2-3 GPa and temperatures of at least 700 °C. Both quartz and coesite are polymorphs with all the members of the Quartz Group that also includes cristobalite, tridymite and stishovite. In Figure 3.1 it is reported a phase diagram of silica.

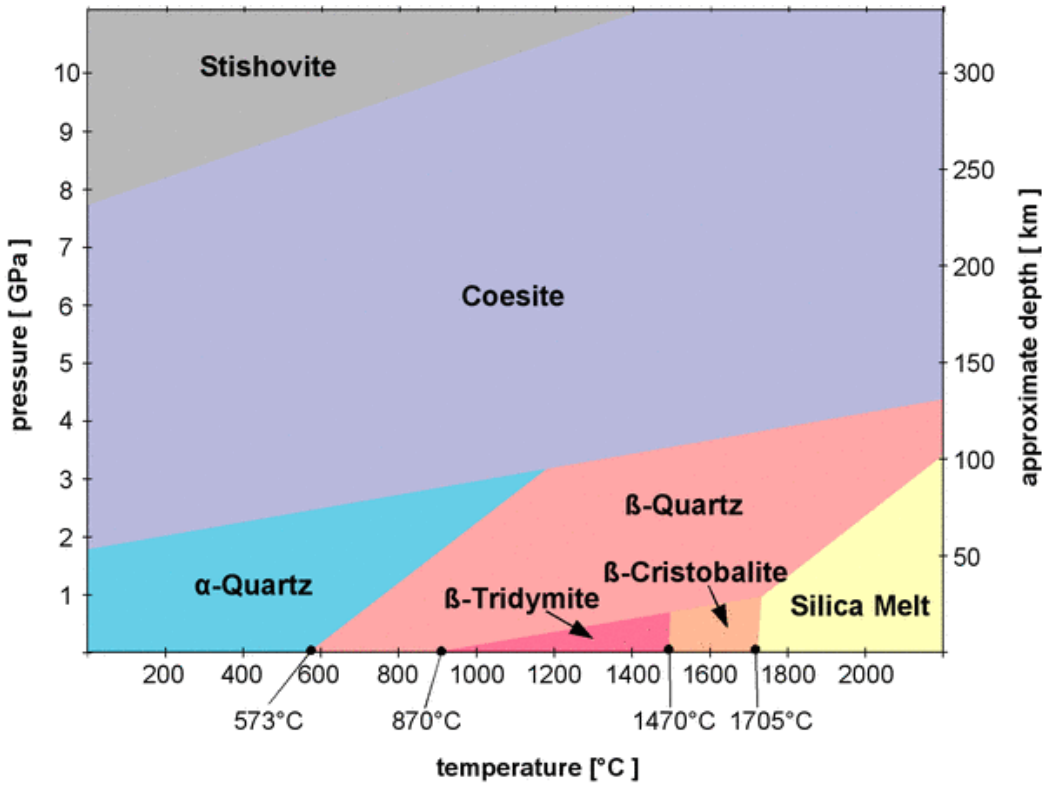

Fig. 3.1: Phase diagram of silica. Data from Hollemann and Wiberg. 1985; Wenk and Bulakh, 2004; Rykart, 1995).

Coesite is a colourless tectosilicate with each silicon atom surrounded by four oxygen atoms in a tetrahedron. Each oxygen atom is then bonded to two Si atoms to form a framework. There are two crystallographically distinct Si atoms and five different oxygen positions in the unit cell. Although the unit cell is close to being hexagonal in shape ("a" and "c" are nearly equal and β nearly 120°), it is inherently monoclinic and cannot be hexagonal. The crystal structure of coesite is

similar to that of feldspar and consists of four-silicon dioxidetetrahedra arranged in Si_4O_8 and Si_8O_{16} rings. The rings are further arranged into chains.

This structure is much more compact than the other members of the quartz group, except stishovite, and is reflected in the higher density and refractive index (2.92 g/cm^3 and 1.594-1.599, respectively). Such structure is metastable at ambient conditions: it will eventually decay back into quartz with a consequent volume increase, but this reaction is very slow at the low temperatures of the Earth's surface because it is a reconstructive phase transition that would imply the breaking of bonds and a complete rearrangement of atoms.

The unit cell is monoclinic (2/m) with space group C2/c. The unit-cell parameters are: $a = 7.1366(2)$ Å, $b = 12.3723(4)$ Å, $c = 7.1749(3)$ Å, ß $= 120.331(2)(°)$ and $V = 546.80(3)$ Å^3 (Angel et al., 2001).

As explained in the previous paragraph, coesite can be found, typically in association with stishovite, in meteor impact zones, within ultrahigh metamorphosed crustal rocks in continental collision areas, or as inclusion in diamonds.

As testified by Coes in 1953, coesite can be relatively easily synthesized in laboratory by applying appropriate pressures and temperatures in a high-pressure device (piston-cylinder press and multi-anvil apparatus are the most commonly used for this purpose). Phase transitions involving coesite are insomuch well known that are generally adopted as pressure calibration standards in the previously mentioned high-pressure instruments.

4. Method for determining the pressure of formation of diamond-inclusion pairs

Diamonds are, as already explained in the first chapter, the only direct samples we have from the deep Earth, but their depths of formation are very poorly constrained. This is principally due to the fact that, being nearly chemically pure, classical geothermobarometers, which rely on the cation partitioning between different minerals or within the same mineral, simply cannot be adopted.

In order to overcome this obstacle, mineral physicists developed the so-called "elastic method". In this new method the formation conditions of diamond can be determined from the residual pressure of inclusions trapped within the diamond, as measured at ambient conditions, and the equations of state (EoS; see Appendix A) of the mineral inclusion and the host diamond (Angel et al., 2014a).

Whether the inclusions are protogenetic, that is they were formed prior to diamond growth, or syngenetic, if they crystallized together with their diamond host, the entrapment conditions can be determined simply from measurements of the residual pressure of the inclusion within the diamond studied at ambient conditions (Zhang, 1998; Izraeli et al., 1999; Sobolev et al., 2000; Howell et al., 2010). This is caused by the fact that the diamond host and its inclusion behave differently in terms of thermal expansion and compressibility. It is easy to think that at the time of entrapment the inclusion and its cavity in the host would have had the same P, T and volume (Howell et al., 2010; 2012). However, due to this contrasting behaviour, the inclusion would expand more on decompression to room conditions than the hole in the diamond. As a consequence, the inclusion undergoes a certain pressure by the surrounding diamond and shows a pressure greater than the ambient pressure.

4.1. The concept of "isomeke"

Starting from the above considerations, now I will explain the simplest way to calculate the pressure of formation of a diamond-inclusion system.

When a diamond-inclusion pair is studied, both are at ambient temperature (T_{end}), the bulk of diamond is at ambient pressure (i.e. zero pressure), while the inclusion is under a uniform small pressure called P_{inc}, which is typically around 0.2-0.4 GPa for olivines (Angel et al., 2014a). This last value is found by comparing the volume of the inclusion still trapped in the diamond with the volume it would have outside of its host. The first volume (V_{int}) comes from the unit-cell parameters of the inclusion. The second (V_{ext}) is obtained knowing the pressure – volume equation of state, which specific for the inclusion under investigation.

If we recompress the system, the hole in the diamond and the inclusion will decrease in size differently. The diamond is stiffer, so the volume of the cavity occupied by the inclusion will be compressed more slowly than the softer inclusion itself, until, at a certain pressure, the diamond hole and the inclusion become equal. This point represents the pressure under which, at ambient temperature, the inclusion fits perfectly with its cavity and is one of the points that

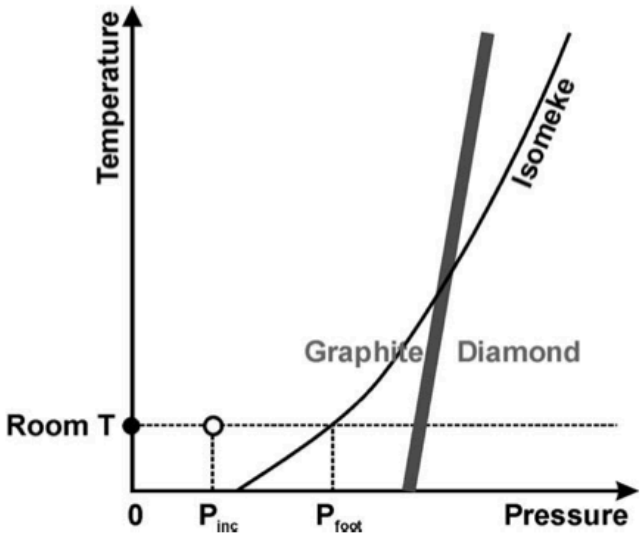

Fig. 4.1: The concept of isomeke. At ambient conditions the inclusion is under a pressure P_{inc}, even though the host is subject to ambient pressure (essentially P = 0). Isothermal compression of the host-inclusion pair leads to them having the same volumes at P_{foot}, which lies on the isomeke. The isomeke is calculated from the EoS parameters of the two phases, and represents the line of possible entrapment conditions for this specific inclusion in its diamond host. At higher temperatures the isomeke passes in to the diamond stability field and represents possible P, T conditions for entrapment of the inclusion by the diamond host (from Angel et al., 2014a).

constitute a curve called isomeke. The isomeke is defined as a line in *P-T* space that represents conditions under which the diamond and inclusion phase would have the same real volumes. It therefore represents the possible entrapment pressure P_E at each temperature. At ambient temperature (T_{end}) the corresponding pressure of the isomeke line is called P_{foot} (Fig. 4.1). This pressure is determined solely by the final inclusion pressure at ambient conditions (P_{inc}) and the isothermal EoS of the diamond and the inclusion.

Since, however, the conditions of P_{foot} and T_{end} are absolutely not realistic because (*i*) diamonds do not grow at 297 *K* in nature and (*ii*) P_{foot} lies, for most inclusions, outside the diamond stability field. For these reasons the path of the isomeke at different pressure and temperature conditions need to be calculated. Being defined as the line along which the volumes of the two phases remain equal, the isomeke's slope is given by $\left(\frac{\partial P}{\partial T}\right)_{isomeke} = \frac{\Delta\alpha}{\Delta\beta}$, where Δα is the difference between the volume thermal expansion coefficients of the diamond and the inclusion and Δβ is the difference in their volume compressibilities. The path of the isomeke in *P-T* space can therefore be calculated away from the point at P_{foot}, T_{end}, by using the EoS parameters of the two phases. If we assume the absence of plastic relaxation (which for lithospheric diamonds can be absolutely reasonable), that could decrease the pressure of the inclusion, and adopt accurate and precise EoS parameters, the calculated isomeke line will pass in to the stability field of diamond, where it will then represent the possible *P-T* conditions for the growth of the diamond (Fig. 4.1).

4.2. The role of elastic relaxation

When a stiff host mineral is exhumed, its softer inclusion, due to its higher tendency to expansion, undergoes a certain pressure. This is a physically unstable "virtual" state because there is a difference in radial stress at the host/inclusion wall that will force the wall outwards. This expansion leads to compression of the host and thus an increase in the radial stress in the host adjacent to the inclusion,

and a relaxation of the pressure inside the inclusion. The resulting expansion of the inclusion continues until the radial stress in the inclusion matches that in the host adjacent to the inclusion (Angel et al., 2014b).

The final observed inclusion pressure is therefore comprised of two parts: $P_{inc} = P_i + \Delta P_{relax}$. Since P_i can be calculated from the EoS of the two phases, the problem of estimating entrapment conditions from observed inclusion pressures lies in the calculation of the change in pressure upon relaxation. Previous estimates of this relaxation have relied on the assumption of linear elasticity theory, however, Angel et al. (2014b) recently proposed a new formulation of the problem that avoids this assumption and allows to calculate ΔP_{relax} only from the volume change and the EoS of the inclusion.

This procedure is already implemented in the EosFit7c program (Angel et al., 2014c), utilized in this work (see Chapter 14) to calculate the *T*-*V* equation of state of coesite, and to perform the isomeke calculation describe in the previous paragraph in order to obtain the pressure of formation of the diamond-inclusion pair.

5. Piston-cylinder apparatus

5.1. Introduction

The piston-cylinder apparatus is a solid media device for generating simultaneously high pressure (up to 6 GPa) and temperature (up to 1700 °C).

The principle of the instrument is to generate pressure by compressing a sample assembly, which includes a resistance furnace, inside a pressure vessel. Controlled high temperature is generated by applying a regulated voltage to the furnace and monitoring the temperature with a thermocouple. The pressure vessel is a cylinder that is closed at one end by a rigid plate with a small hole for the thermocouple to pass through. A piston is advanced into the cylinder at the other hand (Dunn, 1993).

5.2. History

Sir Charles Parsons, a British engineer, was the first to "attack" the problem of generating high pressure simultaneously with high temperature. His pressure apparatus consisted of piston-cylinder devices that used internal electrical resistance heating. He used a solid pressure transmitting material, which also served as thermal and electrical insulation. His cylindrical chambers ranged in diameter from 1 to 15 cm. The maximum pressure at the temperature he reported was of the order of 15000 atm (corresponding to ~1.5 GPa) at 3000 °C.

Loring Coes, Jr., an American chemist at the Norton Company, was the first person to develop a piston-cylinder device with capabilities substantially beyond those of the Parsons device. He did not personally publish a description of this equipment, however, until 1962 (Coes, 1962). The key feature of this device is the use of a hot, molded alumina liner or cylinder. The apparatus is double ended, pressure being generated by pushing a tungsten carbide piston into each end of the alumina cylinder. Because the alumina cylinder is electrically insulating, heating is accomplished, very simply, by passing an electric current from one piston through a sample heating tube and out through the opposite piston. The apparatus

was used at pressures as high as 45000 atm (corresponding to ~4.5 GPa) simultaneously with a temperature of 800 °C. Temperature was measured by means of a thermocouple located in a well. At these temperature and pressure conditions, only one run is obtained in this device, the pistons and the alumina cylinder both being expendable. Even at 30000 atm (corresponding to ~3.0 GPa) the alumina cylinder is only useful for a few runs, as is also the case for the tungsten carbide pistons. The expense of using such a device is great.

Nowadays both the piston and the cylinder are constructed of cemented tungsten carbide and electrical insulation is provided in a different manner than in the device of Coes. In particular, the basis for the modern piston-cylinder apparatus is given by the design described by Boyd and England in 1960 (Boyd and England, 1960), which has been the first machine that allowed experiments under upper mantle conditions to be routinely carried out in a laboratory.

5.3. Theory

It is based on the same simple relationship of other high-pressure devices (e.g. Multi-anvil press and Diamond Anvil Cell):

$$P = \frac{F}{A} \tag{5.1}$$

where P is the pressure, F the applied force and A the area of F application. It achieves high pressures using the principle of pressure amplification: converting a small load on a large piston to a relatively large load on a small piston. The uniaxial pressure is then distributed (quasi-hydrostatically) over the sample through deformation of the assembly materials.

5.4. Components

The main components of the piston-cylinder apparatus (Fig. 5.1) are the pressure generating system, the pressure vessel, and the assembly parts within the vessel. There are two types of piston-cylinder apparatus: non end-loaded and end-loaded, which involve, respectively, one or two hydraulic rams. In the end-loaded

type, used in our experiments and shown in Figure 5.2, the second hydraulic ram is used to vertically load and strengthen the pressure vessel. The non end-loaded type is smaller, more compact and cheaper, and is operable only to approximately 4 GPa.

Pressure is applied to the sample by pressing a piston into the sample volume of the pressure vessel. The sample assembly consists of a solid pressure medium, a resistance heater and a small central volume for the sample. Three common configurations are used: ½", ¾" and 1", which are the diameters of the piston and thus the sample assembly. Accordingly to the pressure amplification concept, the choice of the piston depends on the pressure you need to achieve. In our experiments, due to the very high-pressure conditions to reach, we always used the ½" configuration, except in two cases (runs A701 and B802), for which the ¾" configuration was more appropriate.

During the experiment, water circulates around the pressure vessel, the bridge and the upper plates to cool the system.

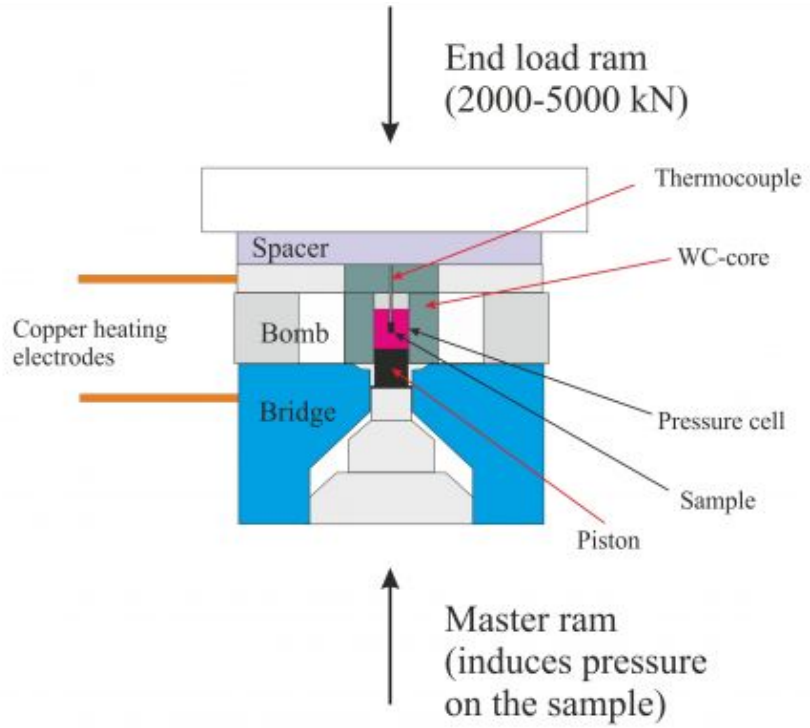

Fig. 5.1: Cross section of a piston-cylinder apparatus.

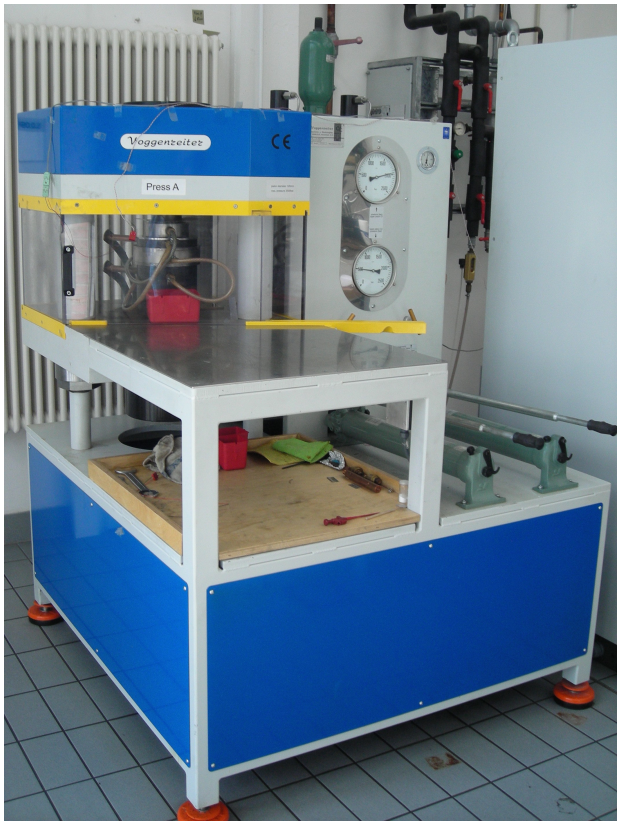

Fig. 5.2: Piston-cylinder apparatus used at Bayerisches Geoinstitut (BGI) (Bayreuth, Germany).

5.4.1. Sample assemblies

The purposes of the sample assembly are to transmit hydrostatic pressure to the sample from the compressing piston, to provide controlled heating of the sample and to provide, via the capsule, a suitable volatile and oxygen fugacity environment for the experiment. Therefore, it includes a component for each of these purposes (Fig. 5.3).

The outer cylinder is a pressure transmitting, electrically insulating cylinder made from NaCl, talc, $BaCO_3$, KBr, CaF_2, or even borosilicate glass. In our experiments, since the low melting point of salt (800 °C) makes it unsuitable at high temperatures, we always used talc. The next components are, in order, an electrically insulating borosilicate glass cylinder, which serves as a trap for water released by dehydration of the talc, and a graphite cylinder, which acts as the "furnace". To locate the sample exactly in the centre of the furnace and to grip the thermocouple (see below for its description), a support rod usually made of

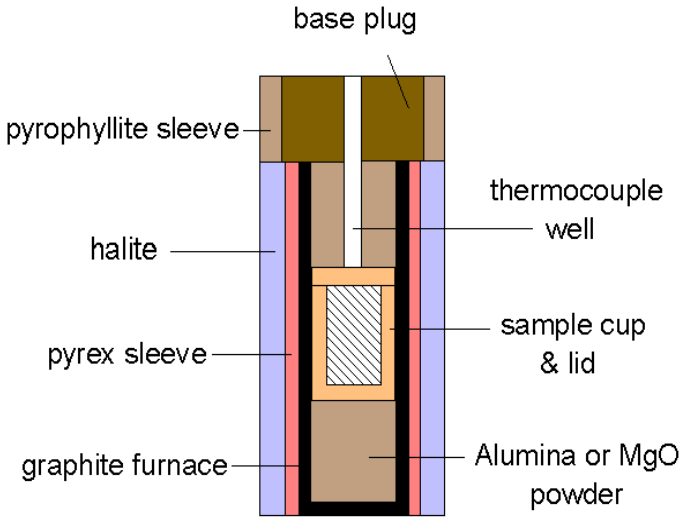

Fig. 5.3: Cross section of a sample assembly for a piston-cylinder press.

crushable ceramics is used. The final component is a conductive steel base plug, located at the top of the sample assembly.

The final part of the assembly is the thermocouple itself, whose wires are insulated from one another and from the material of the assembly by a tube made of mullite. A thermocouple is a temperature-measuring device consisting of two dissimilar conductors that contact each other at one or more spots. It produces a voltage when the temperature of one of the spots differs from the reference temperature at other parts of the circuit. Thermocouples are a widely used type of temperature sensor for measurement and control, and can also convert a temperature gradient into electricity. There are two major types of thermocouples: Pt-Rh thermocouples are more accurate but have an upper temperature limit of about 1950 K; on the other side W-Re thermocouples have larger measurement errors, but are stable at higher temperatures (more than 2250 K) (Dunn, 1993). Each type has three sub-classes: S, R, B for the Pt-Rh type and C, G, E for the W-Re type. In our experiments, due to the temperature range, we always used a S-type thermocouple.

5.4.2. Capsules

The sample capsule must contain the sample and prevent reaction between the sample and the other materials of the sample assembly and not, itself, react with

the sample. It must also be sufficiently weak not to interfere with pressure transmission during the run. For this purpose the materials most used are: Au, Pt, AgPd alloys, Ni and graphite.

Sample volumes are typically 200 mm^3, which translates to ~500 mg of starting material, but with larger assemblies the volume can be up to 750 mm^3.

5.5. Pressure control

The nominal pressure in an experiment can be calculated from the amplification of the oil pressure through the reduction in area over which it is applied, but every component has a characteristic yield stress, consequently the nominal pressure is different from the effective one. Thus, it must be adjusted taking into account the friction:

$$P_{effective} = P_{nominal} + P_{correction}$$

In order to determine the effective pressure, calibration experiments can be done using either static or dynamic methods, and usually make use of known phase transitions (e.g., quartz-coesite transition) or reactions, melting curves or measured water solubility in melts.

Since frictional effects also depend on whether the press is in compression or in decompression, it is good practice to perform the experiments in the same way as the calibration runs.

5.6. Temperature control

Temperature is measured using a thermocouple within an accuracy of ± 1 °C. The accuracy of the temperature is influenced by both random and systematic errors, and is smaller at higher temperature and pressure conditions. Such errors can arise from temperature gradients, differential pressures in the assembly, contamination during the experiment and the effect of pressure on thermocouple electromotive force. These errors can be cushioned choosing the appropriate thermocouple type for the experimental conditions. Temperature gradients, on the other hand, can be minimized using a tapered furnace.

6. Synthesis of material

The synthesis of coesite was carried out at Bayerisches Geoinstitut (BGI) facilities in Bayreuth (Germany), during an eight-weeks research internship in March and April 2014, under the supervision of Dr. Catherine McCammon and with the collaboration of Dr. Tiziana Boffa Ballaran, responsible for the piston-cylinder and X-ray diffraction laboratories, respectively.

Considering the stability field of coesite (Fig. 6.1), both single-crystals and polycrystalline samples were synthesized with a piston-cylinder apparatus, that reaches pressures up to 6 GPa and temperatures up to 1700 °C (for a detailed description of this device see Chapter 5).

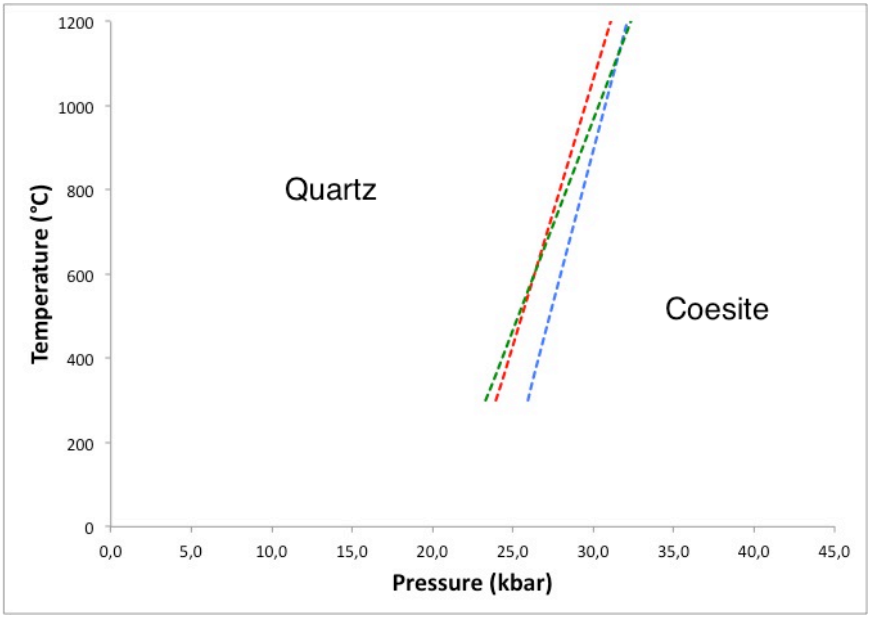

Fig. 6.1: Quartz-coesite transition. Data from Bohlen and Boettcher (1982; red line), Bose and Ganguly (1995; blue line), Hemingway et al. (1998; green line).

6.1. Synthesis of coesite in single crystal

Coesite single crystals were synthesized in one single synthesis route following the procedure described in Angel et al. (2001), with slight differences with respect to this work: run **B794** was performed at a nominal pressure of 4.0 GPa and

800 °C for 72 h (Fig. 6.2) using a talc-pyrex cell assembly. The starting assemblage was powdered natural quartz and 50 µl of water, added with the aid of a syringe, loaded into a Pt capsule. The water-saturated conditions of the run resulted in the synthesis of large (>100 µm) single crystals of coesite. The hydrogen content of the sample was not measured, but is expected to be irrelevant due to the incapacity of coesite to incorporate more than ~22.73 wt. ppm H_2O at typical UHP metamorphic pressures (Mosenfelder, 2000).

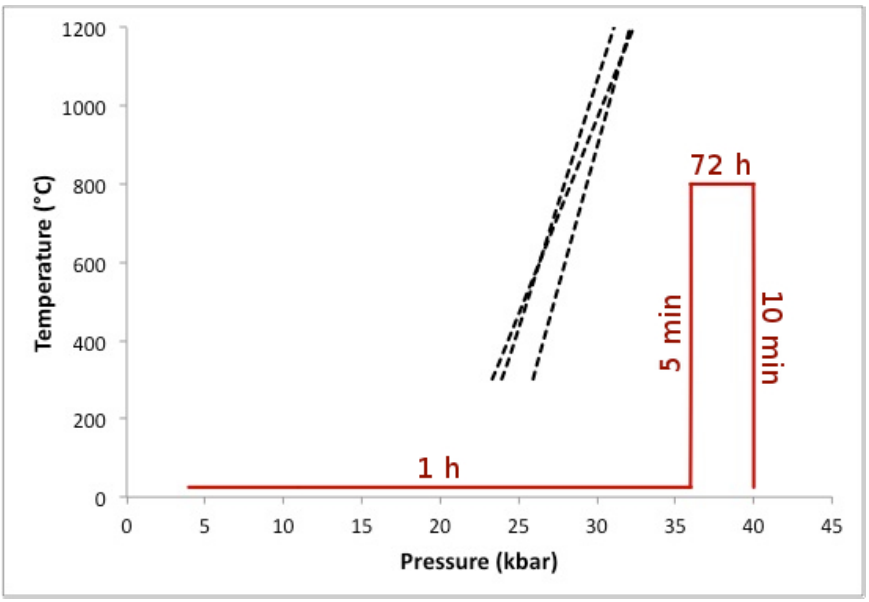

Fig. 6.2: *P-T*-t path for run B794. For dashed lines' references see Fig. 6.1.

6.2. Polycrystalline samples

In order to obtain a polycrystalline sample suitable for RUS measurements (see § 8.4.3.), six experiments (summarized in Table 6.1) were in total performed, using different run conditions and starting materials.

Four preliminary experiments (runs C305, D304, D305 and D306) were carried out with the aim to obtain a considerable amount of coesite available as starting material for subsequent runs.

All of those preliminary runs were performed using a talc-pyrex cell assembly and 99.99% SiO_2 powder (Chempur 290713) loaded into a Pt capsule as starting

material. For the last run (D306) 50 μl of water were also added to the capsule to catalyse the reaction. In all the cases the maximum pressure was 3.5 GPa and the maximum temperature was 1200 °C, following a typical experimental petrology ("cook and look") path for sample recovery at ambient conditions.

For runs C305 and D306 pressure was not maintained due to a non-well identified technical failure and subsequently PXRD on C305 confirmed that only quartz was obtained. As the presence of coesite was instead confirmed for samples D304 and D305, they were ground in an agate mortar under alcohol to a fine-grained (2-5 μm) homogeneous powder and then mixed to obtain a suitable amount of material, called CC01.

The subsequent seven experiments were carried out with the specific purpose to obtain a sample suitable for RUS measurements, adopting a hot-pressing technique similar to that developed by Gwanmesia et al. (1990; 1993) and Gwanmesia and Liebermann (1992) for ultrasonic experiments. To be suitable for ultrasonic techniques like RUS, indeed, the hot-pressed specimen must be free of pores and microcracks and preferred orientation of grains (Gwanmesia et al., 1993). Furthermore, the high-pressure phase should have a uniform chemical composition and crystal structure and the grains should be sufficiently fine so that ultrasonic experiments can be performed at sufficiently high frequencies to minimize dispersion caused by diffraction effects from grain boundaries and energy reflection from the side walls of the specimen. The elastic properties of such a specimen would then be those for a fully dense, elastically isotropic material.

Hot pressing involves the simultaneous application of pressure and temperature to densify powders. The advantage of hot pressing is not only (a) the possibility to synthesize high-pressure and high-temperature phases, but also (b) the capability to obtain a fully dense sample, thanks to plastic deformation triggered by high temperature. On the other side, the disadvantages are the possible (*i*) development of both fractures and (*ii*) preferential orientation of grains due to uniaxial stress, (*iii*) grain growth due to high temperature, (*iv*) formation of porosity and cracks

during decompression. In this discussion we use the term "hot-pressing" loosely to describe all processes of densification regardless of whether the starting material undergoes phase transformation or not.

The starting point for our experiments was the successful *P-T* path described by Gwanmesia (considered the "king of hot-pressing") et al. in 1990 and labelled S1 in Figure 6.3 (Li, 1993). After numerous attempts they defined a path where the sample is first compressed and heated to the stability field of the desired high-pressure phase; subsequently it is decompressed and cooled in three steps: (1) temperature and pressure are first released slowly, but simultaneously, and care is taken to stay within the stability field of the obtained high-pressure phase until the temperature is sufficiently low to avoid a back transformation during decompression. (2) The sample is then held to a constant temperature while pressure is decreased below a certain value, after which (3) pressure and temperature are again decreased simultaneously to recover the sample to ambient conditions. The objective in utilizing this complex *P-T-t* path is to relax intergranular stresses in the polycrystalline aggregates (Gwanmesia et al., 1993).

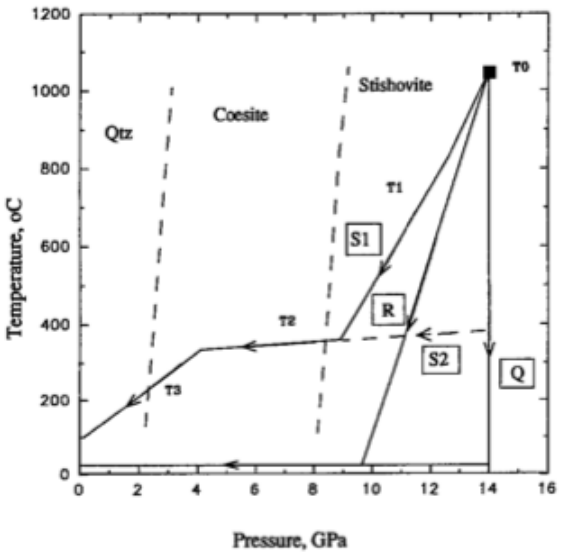

Fig. 6.3: *P-T* paths with arrows for hot pressing and recovering high-quality polycrystals of SiO_2-stishovite (from Li et al., 1996).

All of the experiments performed with this technique were carried out using a talc-pyrex cell assembly, whether with ½" or ¾" configuration, depending on the pressure achieved, and alumina sleeve and disks. The thermocouple used was a S-type, due to the relatively low temperature achieved (≤ 1200 K), and the capsule made of platinum was whether 5 or 3.5 mm in diameter, depending on the starting material.

For run **A689**, CC01 powder was cold pressed and the pellet obtained was lead to 3.5 GPa and 1000 °C, as shown in Figure 6.4.

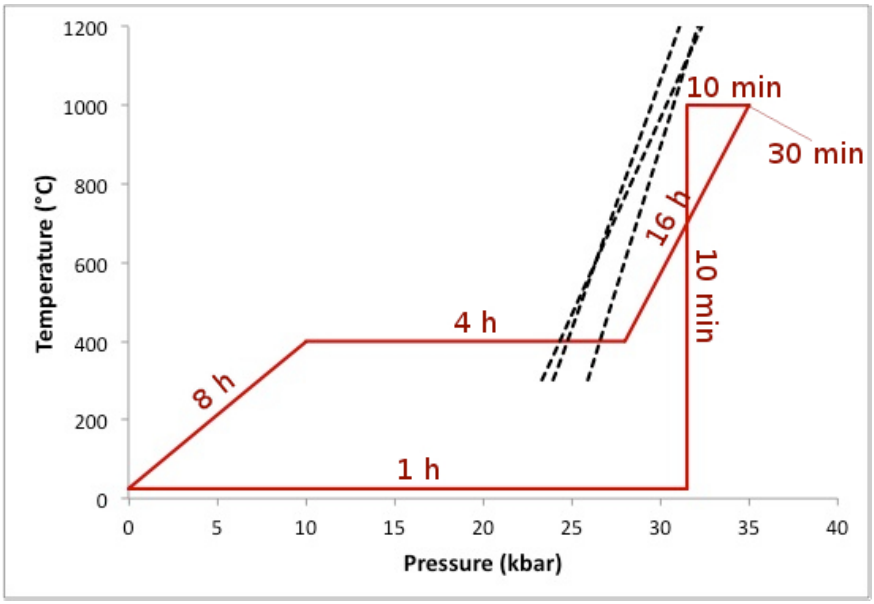

Fig. 6.4: *P-T*-t path for run A689. For dashed lines' references see Fig. 6.1.

The resulting sample was observed with SEM and showed fractures parallel to the axis of the cylindrical specimen (see Fig. 7.3a). This was probably due to the release in strain energy: when a freshly hot-pressed polycrystalline sample is cooled and decompressed, in fact, strains are set up around the grain boundaries because of differential thermal contraction and isothermal decompression along various crystallographic axes due to crystal anisotropy. At high temperatures these strains can be relieved by mechanisms such as plastic flow, grain boundary sliding

and by diffusion processes, but at lower temperatures the strains are "frozen-in" and increase as the temperature falls (Gwanmesia et al., 1990), causing cracks.

Based on these observations, the starting material was modified in order to avoid the formation of cracks during decompression, following the procedure adopted by Li et al. in 1992 to minimize the volume reduction that occurs due to transformation from the low-pressure to the high-pressure phase. A dense fused silica rod of external diameter comparable to the internal diameter of the Pt capsule was thus used for next experiments.

Both runs **A695** and **A697** were carried out loading a Pt capsule with a SiO_2 glass rod of ~5 mm in diameter. Graphite powder was also added above and below capsule in order to further amortize the stress fall. The capsule was lead to a maximum pressure of 4 GPa and to a maximum temperature of 1200 °C, however, while for run A697 the *P-T* path was completed with a slow cooling followed by two slow decompressional steps (Fig. 6.6), during run A695 thermocouple broke. The power was hence set on the basis of previous experiments to achieve more or less the target temperature, but without maintaining a direct control on temperature during cooling. After 15 hours at peak

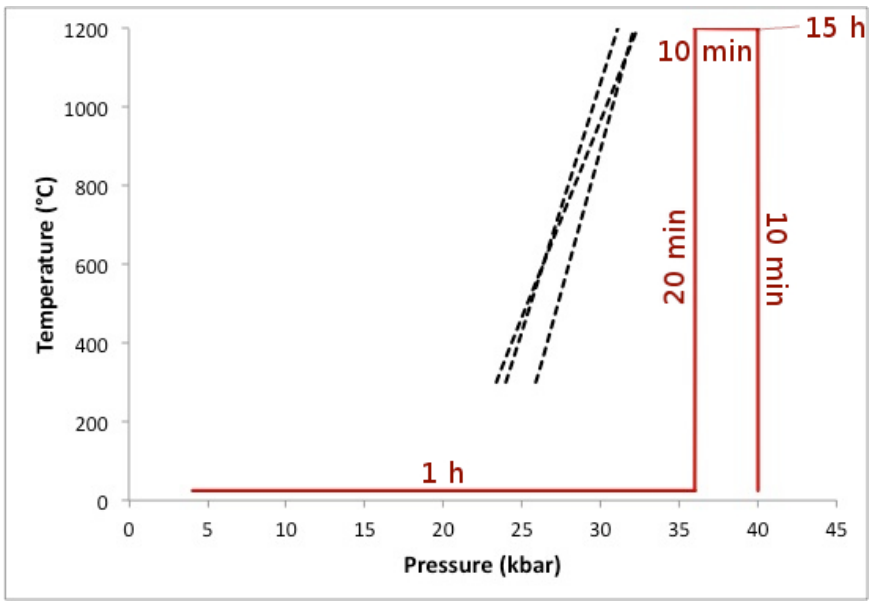

Fig. 6.5: *P-T*-t path for run A695. For dashed lines' references see Fig. 6.1.

conditions, therefore, the system was quenched (Fig. 6.5).

Considering that PXRD analysis on A695 sample (see Fig. 7.5a), in which the peak conditions had been maintained for 15 hours, verified the presence of big crystals of coesite rather than fine grains, for run A697 the peak conditions were maintained only for 10 minutes. In spite of this improvement, again PXRD analysis (see Fig. 7.5b) confirmed that crystallites were too big for a RUS measurement, probably owing to the high reactivity of silica amorphous glass, that grows very quickly at high pressure and temperature.

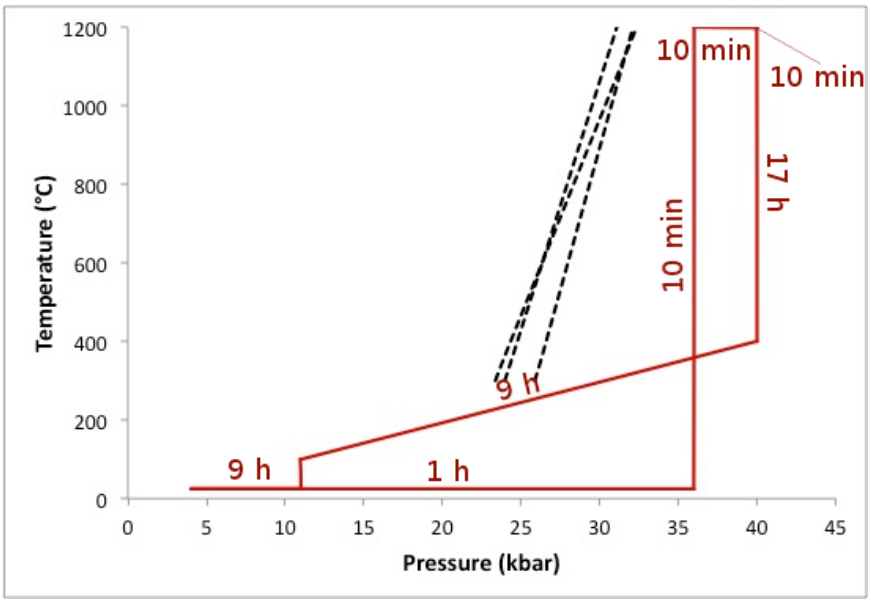

Fig. 6.6: *P-T*-t path for run A697. For dashed lines' references see Fig. 6.1.

For the next two runs it was therefore decided to go back to the previous starting material, CC01, and try to hot press it staying in the stability field of quartz, to avoid the growth of coesite powder. Runs **A701** and **B802** had exactly the same conditions: the capsule was lead to a peak pressure of 1.6 GPa and to a peak temperature of 600 °C, and then slowly decompressed to ambient conditions (Fig. 6.7). In both of the cases, however, the sample obtained was not sufficiently dense for RUS measurements, due to *P-T* conditions anomalously low for a hot pressing.

PXRD analysis on A701 sample, moreover, confirmed the presence of zircon (see Fig. 7.6) due to contamination, which precluded the possibility to use again CC01 material.

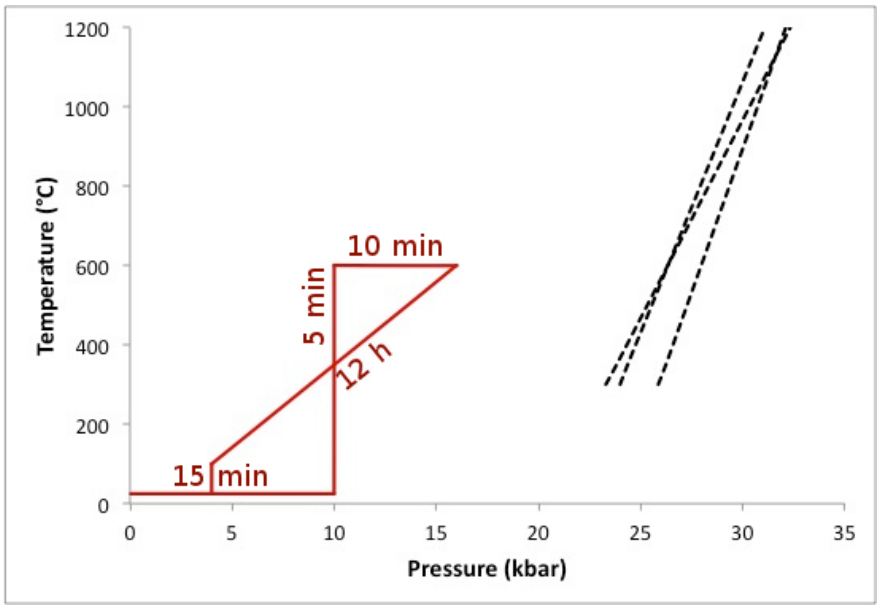

Fig. 6.7: *P-T*-t path for runs A701 and B802. For dashed lines' references see Fig. 6.1.

For the last run (**B803**) was thus decided to use the material obtained from run A697, which, considering the PXRD analysis (see Fig. 7.5b), was pure coesite. It was preliminarily ground with agate mortar under alcohol in a very fine (2-5 μm) homogeneous powder and then loaded in a Pt capsule of 3.5 mm in diameter. Also in this case graphite powder was added above and below capsule. Considering that samples from runs A701 and B802 were too soft, for this last run the path was modified trying to find the best compromise between *P-T* conditions sufficiently high for a hot pressing, but not too high to avoid the growth of grains. Relying on the study on kinetics of the coesite-quartz transition by Perrillat et al. (2003), the following path was defined (Fig. 6.8).

First, the maximum pressure of 3.3 GPa and the maximum temperature of 800 °C were reached as soon as possible to avoid the growing of crystallites. Then,

temperature was decreased very slowly (29.412 °C/h) to prevent the formation of microcracks because of stress release. When a temperature sufficiently low (300 °C) to cross the phase boundary without the risk of a back transformation to quartz was reached, temperature and pressure were simultaneously decreased during a 9 hours long ramp. Both cooling and decompression rates were very slow (6.06 °C/h and 2.44 kbar/h, respectively) again in order to prevent the formation of cracks and porosity. Once the value under which the automatic control on temperature is not possible anymore (100 °C) was reached, the system was quenched. Finally, a second 9 hours long decompression was applied in order to limit the formation of cracks in the newly formed "cold" system.

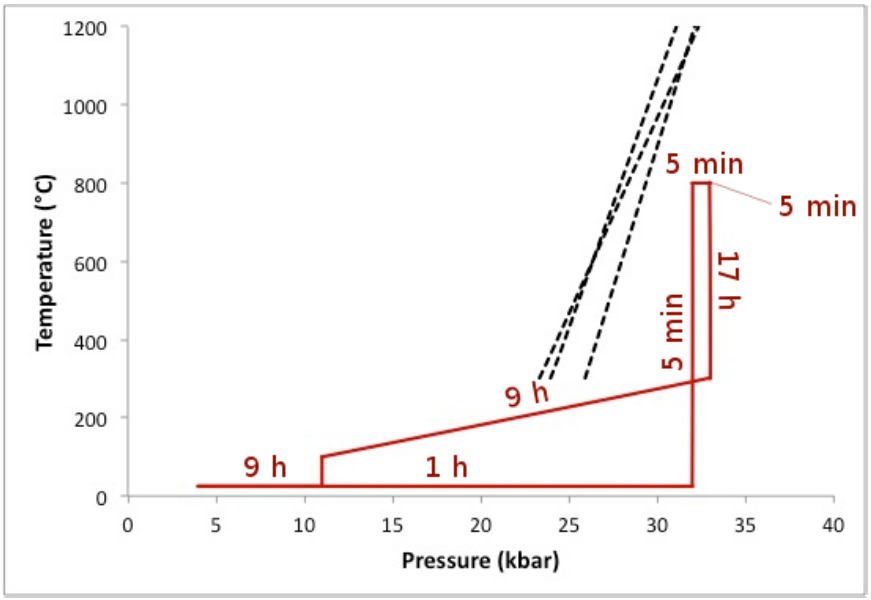

Fig. 6.8: *P-T*-t path for run B803. For dashed lines' references see Fig. 6.1.

Tab. 6.1: Summary of experiments done in order to obtain a sample suitable for RUS measurements. All of these runs were performed at BGI facilities (Bayreuth, Germany).

NAME	DATE	PRESS	ASSEMBLY	BOMB	SLEEVE + DISKS	TC	STARTING MATERIAL	CAPSULE	P/T CONDITIONS	NOTES	RESULT
A689	14/03/2014	A	½" talc/pyrex	N	Al_2O_3	S-type	CC01 cold pressed to pellet	3.5 mm Ø Pt	3.5 GPa 1000 °C		Coesite + extraphase; Longitudinal fractures
A695	28/03/2014	A	½" talc/pyrex	N	Al_2O_3	S-type	SiO_2 glass rod	5 mm Ø Pt + graphite powder	4.0 GPa 1200 °C	TC broken, set power to 1142 kV	Giant crystals of coesite
A697	03/04/2014	A	½" talc/pyrex	N	Al_2O_3	S-type	SiO_2 glass rod	5 mm Ø Pt + graphite powder	4.0 GPa 1200 °C		Giant crystals of coesite
A701	11/04/2014	A	¾" talc/pyrex	6	Al_2O_3	S-type	CC01	3.5 mm Ø Pt + graphite powder	1.6 GPa 600 °C		Coesite + extraphase; too soft
B802	20/04/2014	B	¾" talc/pyrex	6	Al_2O_3	S-type	CC01	3.5 mm Ø Pt + graphite powder	1.6 GPa 600 °C	Servo error	Coesite + extraphase; too soft
B803	24/04/2014	B	½" talc/pyrex	S	Al_2O_3	S-type	A697	3.5 mm Ø Pt + graphite powder	3.3 GPa 800 °C	Servo error	Coesite polycrystalline

7. Samples characterization

7.1. Single crystals

The synthesis run carried out to obtain single crystal material (**B794**) was successful and the samples obtained (Fig. 7.1) were characterized (1) by microRaman spectroscopy to verify their complete transformation to coesite; and (2) by SCXRD to find some crystals suitable for the in-situ high-temperature X-ray diffraction (e.g., crystal quality evaluated on diffraction profiles, absence of twinning, sharp optical extinction). The first analysis was performed at BGI, the second at the Department of Geosciences of University of Padova.

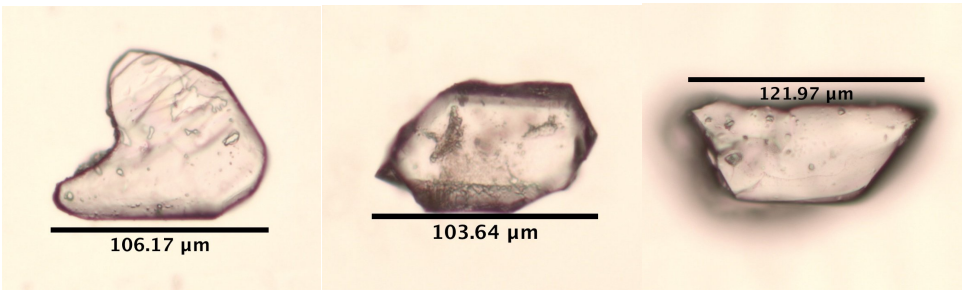

Fig. 7.1: Three single crystals of coesite obtained in this work.

7.1.1. MicroRaman spectroscopy

In order to verify the complete transformation to coesite, and, eventually, the presence of a residual amount of quartz in our single crystals, a preliminary check by microRaman spectroscopy was done. The microRaman spectrometer used was a *Horiba Scientific Inc.* instrument equipped with a 632.8 nm laser; a 50x objective was used with a spot size of about 1 µm. Four crystals were analysed randomly and their Raman spectra are shown in Figure 7.2. The main four peaks of our coesite are evident at 520, 270, 466 and 178 cm^{-1}, in excellent agreement with literature data (Hemley, 1987). A further peak at 118 cm^{-1} was not identified. It needs to be noticed that the peak at 466 cm^{-1} is in perfect overlap with the main peak of quartz at 464 cm^{-1}. Even if it is not possible, in absence of high-pressure

data as comparison, to discern if it belongs to coesite or if it results from quartz contamination, its intensity is extremely low, indicating in any case a very minor amount of quartz.

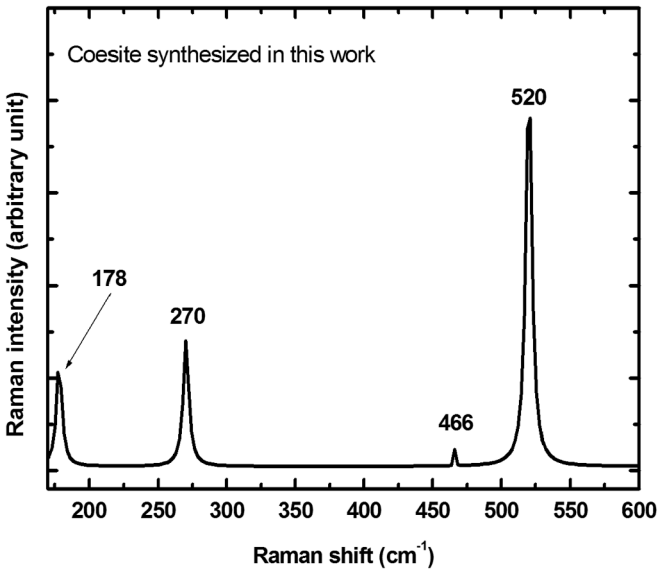

Fig. 7.2: A typical microRaman spectrum of the single crystals synthesized in this work. It shows the main three peaks of coesite already reported in literature data (i.e. Hemley, 1987).

7.1.2. Single-crystal X-ray diffraction

In order to evaluate the crystal quality of coesite synthesized in this work the sample was analysed by single-crystal X-ray diffraction. The measurement on the single crystal was carried out using a new worldwide-assembled single-crystal X-ray diffractometer *Supernova* (*Agilent Technologies*), equipped with a *Pilatus 200K Dectris* area detector and installed at the Department of Geosciences in Padova. The unit-cell parameters obtained were: a = 7.138(2) Å, b = 12.373(1) Å, c = 7.121(1) Å, β = 119.57(2) (°), V = 547.01(17) $Å^3$. The unit-cell volume differs by only 0.05 Å (lower than the experimental error) with respect to literature data (Ikuta et al., 2007).

7.2. Polycrystalline samples

The characterization of polycrystalline samples was performed at BGI, except for the SEM and EBSD analyses of run B803, carried out at the Department of Geosciences in Padova.

A piece of **A689** sample was observed using a *Leo 1530 Gemini* with field emission electron gun. Since this was only a check, in order to improve next experiments, the sample preparation was particularly expeditious: 1) the sample was first glued on a piece of epoxy; 2) then a cylinder made of graphite was glued around the sample and a mixture constituted by 2/3 of resin and 1/3 of hardener was spilled in the graphite cylinder; 3) after 12 hours of drying the specimen was polished by abrasive silicon carbide (SiC) paper and coated with graphite.

The SEM image of A689 sample (Fig. 7.3a) shows a set of longitudinal fractures, parallel to the major axis of the capsule. The BSE image (Fig. 7.3b) shows instead a pervasive porosity throughout the surface of the specimen. Both cracks and pores were probably due to the release in strain energy occurred during decompression and cooling and indicated that run conditions had to be revisited.

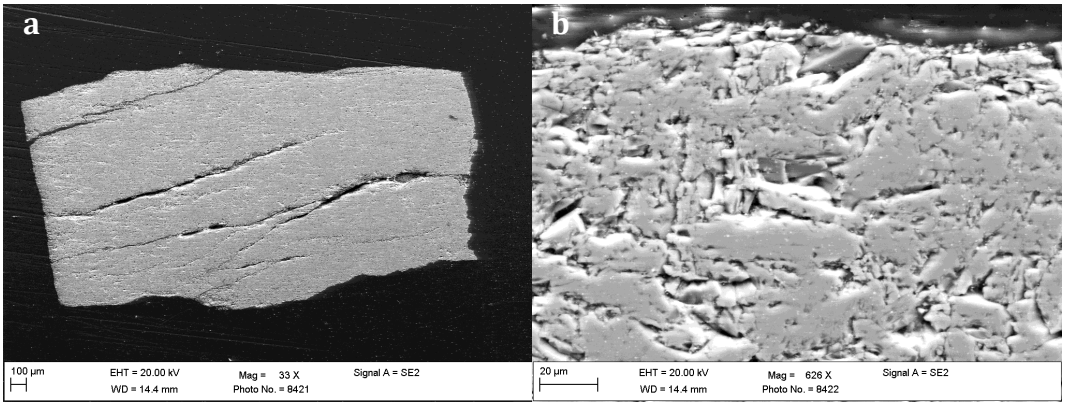

Fig. 7.3: a) SEM image of A689 sample; b) BSE image of A689 sample.

The other part of the same sample was ground in agate mortar under alcohol in a fine grained homogeneous powder and analyzed by a *X'Pert Philips* X-ray powder diffractometer using the CoKα radiation (1.7902 Å) between 15 and 90 ° in 2θ, with 0.03 ° step, 40 kV and 40 mA. The resulting diffractogram is shown in Figure 7.4 and confirms that material is still coesite, with other minor quantities of quartz and zircon. Quartz formed because of a back transformation from coesite at high temperature; zircon was, instead, an extra phase present in the starting material used to perform syntheses C305, D304, D305 and D306.

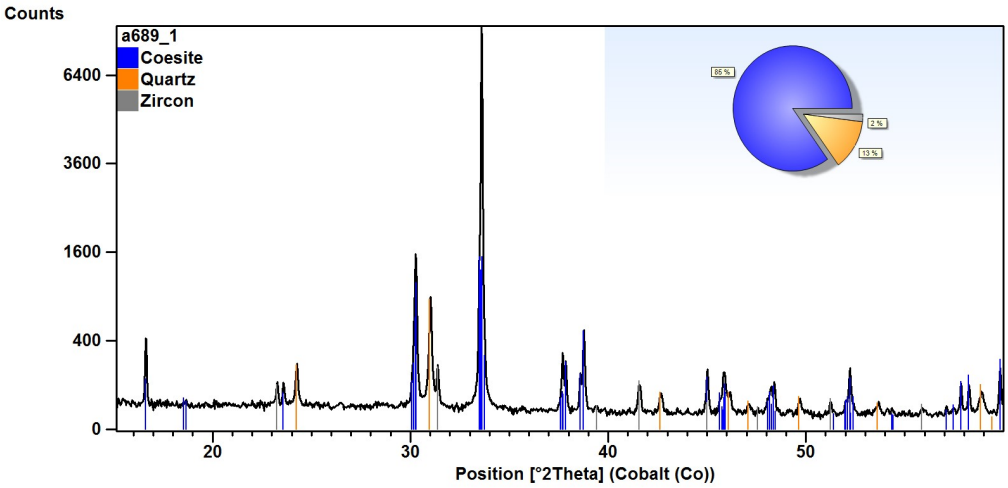

Fig. 7.4: X-ray powder diffractogram of A689 sample. In the top right part of the diffractogram there is a pie diagram representing the proportion of components in the sample, basing on a semi-quantitative refinement.

Products of runs **A695** and **A697** were analysed without any preparation by a *D8 Discover Bruker* X-ray powder diffractometer using the CoKα radiation (1.7902 Å) between 25 and 85 ° in 2θ, with 30 ° step, 40 kV and 40 mA. The presence of spots rather than circles confirmed the presence of big crystals of coesite, and their diffractograms are shown in Figure 7.5a,b.

The cylinder obtained from run **A701** was very soft and one of its pieces was ground under alcohol in an agate mortar and then studied with the *X'Pert Philips*

X-ray powder diffractometer using the CoKα radiation (1.7902 Å) between 15 and 90 ° in 2θ, with 0.03 ° step, 40 kV and 40 mA. The resulting diffractogram is reported in Figure 7.6. By making a comparison of our peaks to international databases we could identify quartz, cristobalite and zircon in addition to coesite. Quartz and cristobalite formed because of a back transformation from coesite triggered by high temperature. Zircon, instead, was an unwelcome extra phase already present in the starting material.

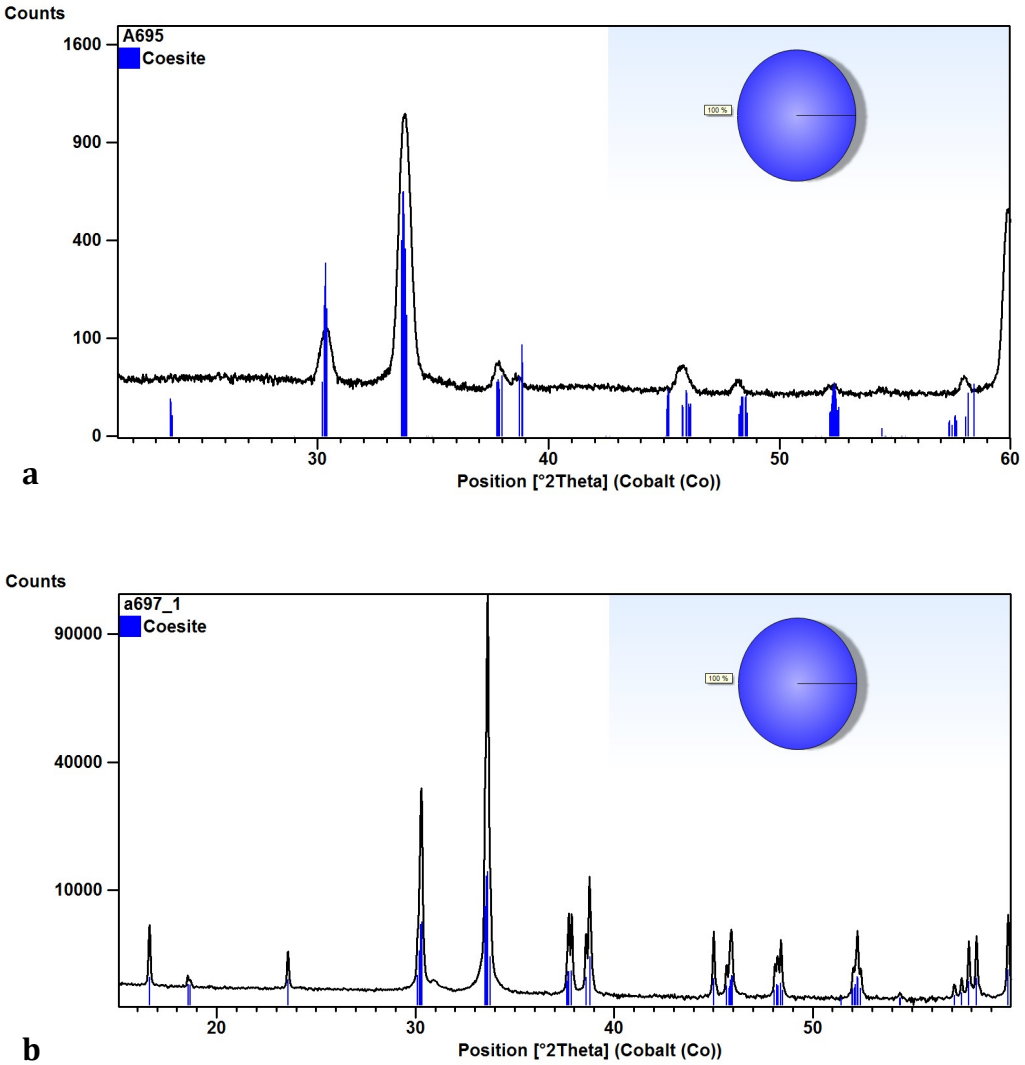

Fig. 7.5: X-ray powder diffractograms of a) A695 and b) A697 samples, respectively. In the top right part of both the diffractograms there is a pie diagram representing the proportion of components in the sample, basing on a semi-quantitative refinement.

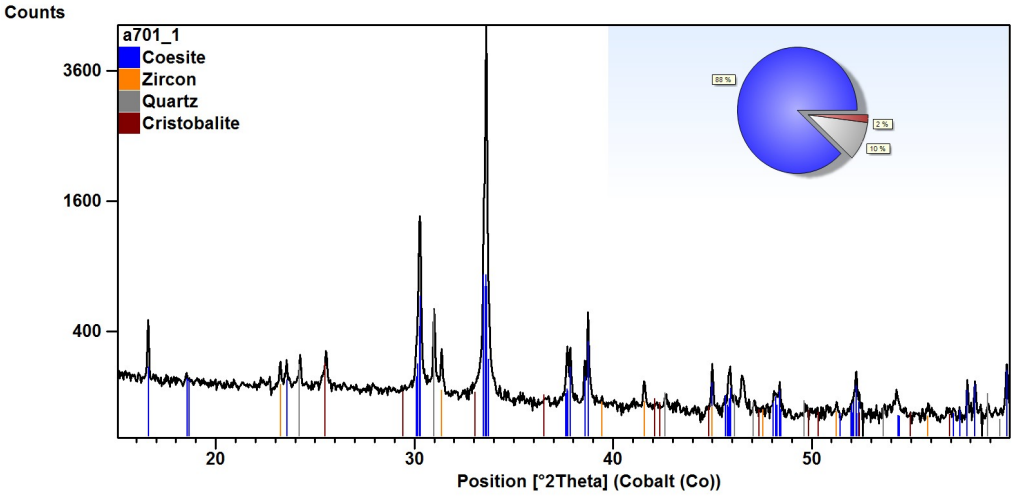

Fig. 7.6: X-ray powder diffractogram of A701 sample. In the top right part of the diffractogram there is a pie diagram representing the proportion of components in the sample, basing on a semi-quantitative refinement.

The synthesis product of run **B803** was preliminarily measured using the *D8 Discover Bruker* X-ray powder diffractometer using the CoKα radiation (1.7902 Å) between 25 and 85 ° in 2θ. In Figure 7.7 the diffractogram of our coesite is shown. It was thus considered suitable for RUS measurements and was then cut in a cylinder of ~1 mm in diameter and ~0.5 mm in height (Figg. 7.8a,b).

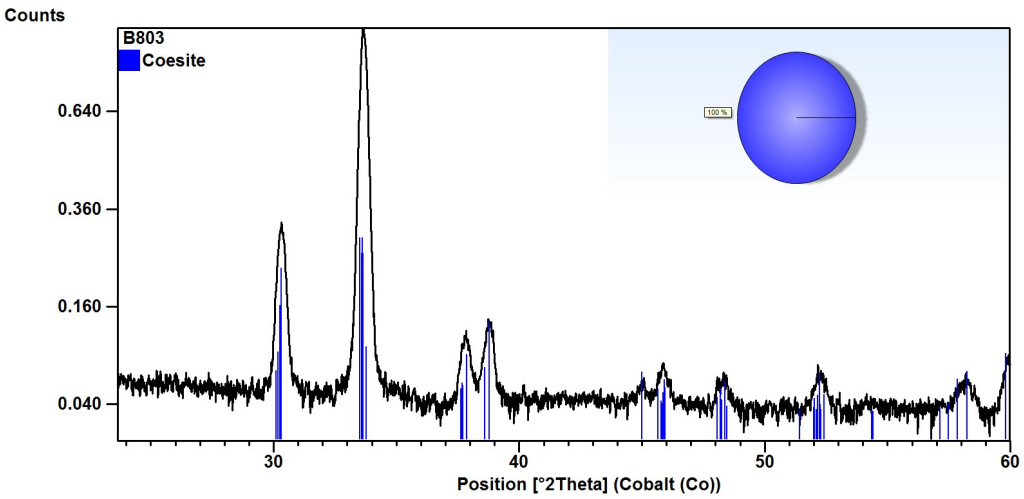

Fig. 7.7: X-ray powder diffractogram of B803 sample. In the top right part of the diffractogram there is a pie diagram representing the proportion of components in the sample, basing on a semi-quantitative refinement.

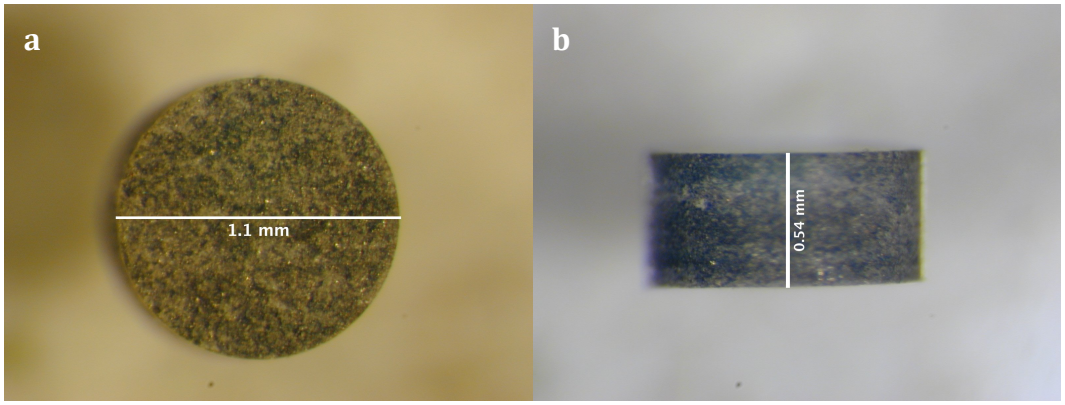

Fig. 7.8: a) Upper and b) lateral view of the polycrystalline cylinder of coesite cut out directly from the B803 capsule.

However, before sending the sample for RUS measurements, it was analysed by SEM in order to verify the general porosity, grain size and presence of cracks, and, subsequently, by EBSD in order to verify the grain orientation. All these parameters, in fact, can affect the final RUS results, as it is explained in detail in § 8.3..

The EBSD technique is the diffraction at SEM by using backscattered electrons and can provide important information about the lattice planes orientation and accordingly about the grain orientation. Accelerated electrons in the primary beam of a SEM, in fact, can be diffracted by atomic layers in crystalline materials. These diffracted electrons can be detected when they impinge on a phosphor screen and generate visible lines, called Kikuchi bands, or "EBSP's" (electron backscatter patterns). These patterns are effectively projections of the geometry of the lattice planes in the crystal, and they give direct information about the crystalline structure and crystallographic orientation of the grain from which they originate. When used in conjunction with a database that includes crystallographic structure information for phases of interest and with software for processing the EPSP's and indexing the lines, the data can be used to identify phases based on crystal structure and also to perform fabric analyses on polycrystalline aggregates.

The preparation for SEM and EBSD analyses, performed at the Department of Geosciences in Padova, was very hard due to the minimal size of the sample and to its easy disintegration. The sample was preliminary incorporated in Araldite® 20/20, an epoxy resin constituted by ten parts by weight of resin and three parts

by weight of hardener, within a sample holder made by Teflon®. After at least one minute of mixing, a vacuum impregnation by a *Struers CitoVac* was performed. After at least 12 hours in oven at 40 °C the sample was released from its sample holder, signed, and polished in a four-steps procedure. (1) LAPPING: first, the sample was polished manually by using SiC sandpaper water-lubricated in a *Struers LaboPol-5* to uncover its surface. Then, it was again polished manually on glass discs of one centimetre height: the first step was done with 500 mesh SiC powder mixed with water, the second with 800 mesh SiC powder mixed with water. (2) PRE-POLISHING: secondly, the sample was further polished with a 1200 mesh SiC powder-water mixture. (3) POLISHING: the sample was subsequently polished by using diamond suspensions in two-steps of at least five minutes each. The first step was performed using a 6 μm diamond suspension, the second using a 3 μm diamond suspension. Both of these steps were performed by a *Struers LaboPol-35*, making use of a 2.5 N weight, a silk cloth (*ATM Gamma* polishing cloth) and with 250 rpm. (4) SUPERPOLISHING: this last step was performed by using a *VibroMet 2* (*Buehler*) with the specific purpose to make the sample suitable for EBSD analysis. The instrument was provided with a MasterTex® cloth and the polishing suspension used was a non-crystallizing colloidal silica MasterMet® 2 (pH=10.5 and 0.02 μm). The superpolishing was performed during more consecutive nights in order to reduce the porosity, to reorder the crystalline structure of the sample and to minimize the metallization afterwards.

The sample was studied using a *CamScan MX3000* with LaB_6 source. The overview of the sample obtained by SEM (Fig. 7.9) shows that there is a minimal

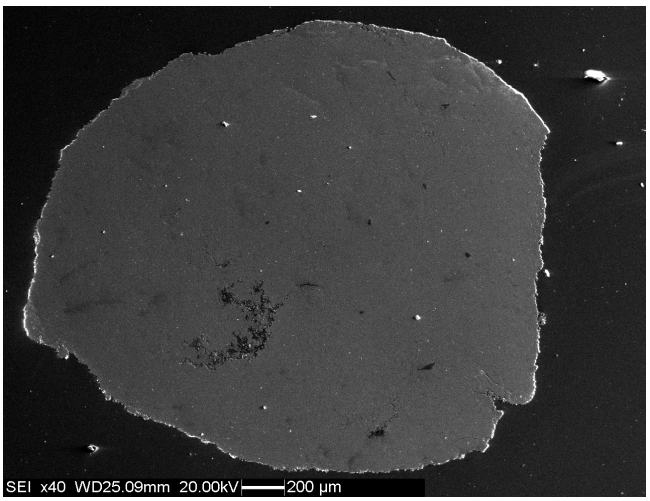

Fig. 7.9: SEM overview of B803 sample. The dark matter in the left bottom part is resin residual from preparation.

amount of fractures, localized only in the outer part of the sample. This is due to the fact that the outer surface had been in direct contact with the Pt capsule and this had exerted a certain stress on it.

The BSE image of the sample (Fig. 7.10a) shows that the grain size is in average 5 μm, that no evident cracks are present and that at the same time the sample is not characterized by significant porosity. In addition, on the same Figure in yellow we reported the points where the EBSD technique was used and the results of it are shown in Figure 7.10c by the Kikuchi lines. Such lines were then indexed by coesite diffraction pattern (Fig. 7.10d) and the final results have been plotted in pole figures (Fig. 7.10b). These figures clearly show that there is not any preferred crystallographic orientation and thus we considered this coesite sample definitively suitable for RUS measurements.

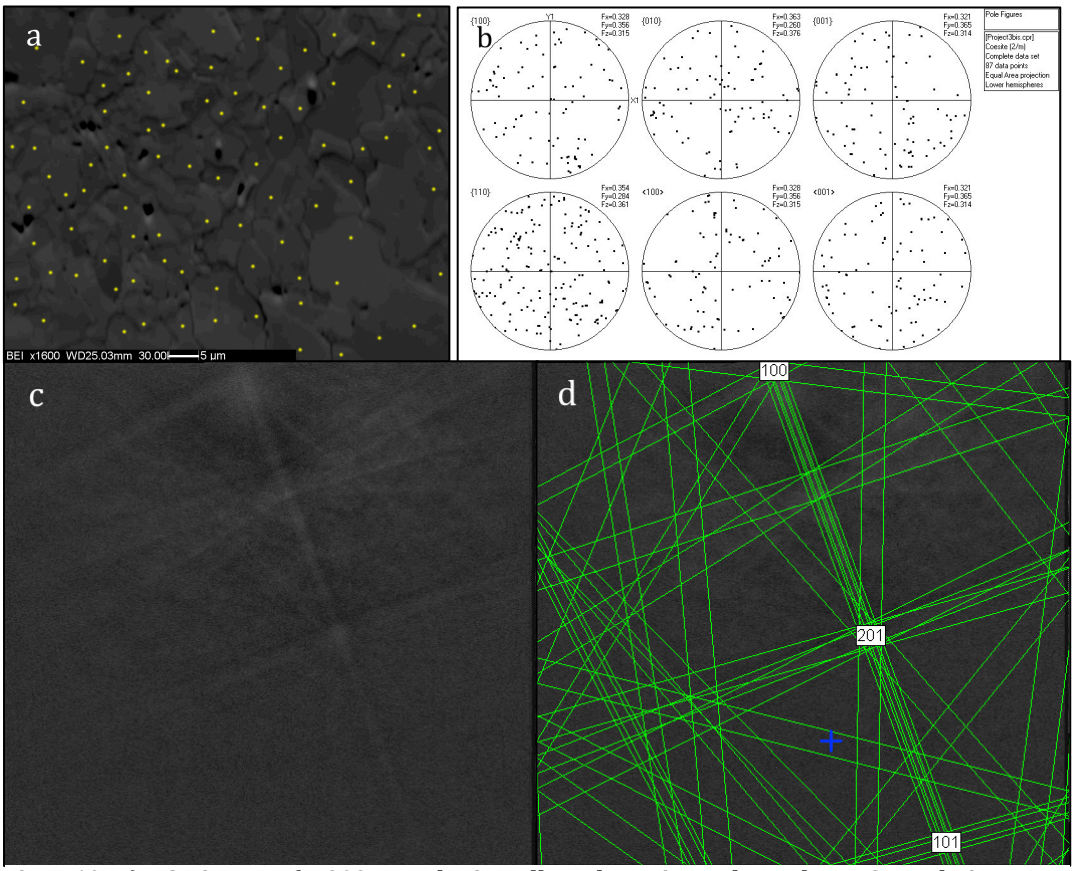

Fig. 7.10: a) BSE image of B803 sample; in yellow the points where the EBSD technique was applied; b) Pole figures highlight that grains have no preferential orientation; c) Kikuchi pattern of one yellow point; d) Kikuchi lines indexed according to coesite diffraction pattern.

8. Resonant Ultrasound Spectroscopy

8.1. Introduction

Resonant ultrasound spectroscopy (RUS) is a laboratory technique used for measuring fundamental material properties involving elasticity. This technique relies on the fact that solid objects have natural frequencies at which they vibrate when mechanically excited. The natural frequency depends on the elasticity, the size and the shape of the object; RUS exploits this property of solids to determine the elastic tensor of the material. Compared to light scattering and other ultrasonic methods, the main advantages of RUS are its capabilities for determining a full set of elastic constants with very high internal consistency, and the associated acoustic dissipation, from a single experimental run, even on a sample with low symmetry (other techniques are practically impossible to be used for low symmetry crystals). Other methods require sample realignment and several runs to obtain the full set of elastic constants.

8.2. History

Interest in elastic properties made its entrance with 17th century philosophers, but the real theory of elasticity, indicating that the elastic constants of a material could be obtained by measuring sound velocities in that material, was summarized only two hundreds of years later. In 1964, D. B. Frasier and R. C. LeCraw used the solution calculated in 1880 by G. Lamè and H. Lamb to solve the forward problem, and then inverted it graphically, in what may be the first RUS measurement. Nevertheless we had to wait the participation of geophysics community, interested in determining the Earth's interior structure, to solve also the inverse problem: in 1970 three geophysicists improved the previous method and introduced the term resonant sphere technique (RST). Excited by the encouraging results achieved with lunar samples, one of them gave one of his students the task to extending the method for use with cubic samples. This method, now known as the rectangular parallelepiped resonance (RPR) method, was even

more extended by I. Ohno in 1976. Finally, at the end of eighties, A. Migliori and J. Maynard expanded the limits of the technique in terms of loading and low-level electronic measurements, and with W. Visscher brought the computer algorithms to their current state, introducing the final term *resonant ultrasound spectroscopy (RUS)* (Maynard, 1996).

8.3. Overview

RUS is used to measure the normal frequencies of vibration of an object. These depend on the physical symmetry of the object (i.e. its shape), the symmetry of its elastic tensor (which is determined by its crystal symmetry), its density, and its dimensions. A complete RUS analysis, to determine the elastic constants of a material directly from its natural resonances, involves solution of both the *forward* and *inverse* problems. The *forward* problem is to calculate the expected resonance frequencies of each of the normal modes of a sample, given the sample dimensions, mass, density and its elastic constants. The method for doing this, described in detail by Migliori and Sarrao (1997), is to carry out a Lagrangian minimization of the free energy function, using the Rayleigh-Ritz method of eigenvalue approximation, taking powers of Cartesian coordinates as basis functions. The mathematical theory behind this solution was first published by Demarest (1971) and is well explained in Appendix B. Examples of the oscillational eigenmodes that are possible in a rectangular parallelepiped sample are illustrated in Figure B.1. The *inverse* problem is then to work backwards to calculate the elastic constants of the material from the experimentally determined resonance frequencies of the eigenmodes, which can be measured directly using RUS experiments. The method for solving these problems is referred to in much of the literature as the RPR (rectangular parallelepiped resonance) method (Ohno, 1976), as a rectangular parallelepiped is the most common geometry for a RUS sample. Until recently, solutions to the *forward* and *inverse* problems required a relatively large amount of computing power, however this is now possible in just a few minutes using a standard PC. Instrumentation has also benefited from

modern integrated electronics, which enable digital signal processing algorithms (described in detail by Migliori et al., 2001) to acquire the data very quickly.

The first step in solving the *forward* and *inverse* problems is to experimentally measure the natural resonance frequencies of a sample with known dimensions (shape, size and density), using RUS. A rectangular parallelepiped with orthogonal faces is the usual geometry for samples as its dimensions are easily measured, hence reducing the computing time. In principle, though, any shape can be used. The parallelepiped is rectangular, rather than a cube, so that none of the resonances are degenerate and all modes can be observed individually. In reality, it is extremely difficult to produce an exactly cubic sample anyway, but a parallelepiped with significantly different edge lengths will yield a RUS spectrum where resonance peaks are more widely distributed (and therefore easier to measure) than an almost cubic sample. Optimum dimensions for the parallelepipeds used in the following experiments are of the order of a few mm, to compare with the size of the transducers.

After resonance frequencies have been measured, the rest of the RUS analysis is entirely computational. The *forward* problem is solved first by inputting dimensions, mass, and well-informed guesses of the elastic constants into the RPR fitting procedure (Migliori and Sarrao, 1997). This produces a list of the expected resonance frequencies. These calculated frequencies are then compared to the list of experimentally measured frequencies, using the Levenberg-Marquardt algorithm (Migliori and Sarrao, 1997; Migliori et al., 2001) to carry out a least-squares fitting procedure between the two, with the only variable parameters being the elastic constants. The solution to the *inverse* problem, i.e. convergence of this fit, then produces the experimentally determined elastic constants. A good convergence can only be achieved if several conditions are met (Migliori and Sarrao, 1997):

1. The sample must be well prepared: homogeneous and without cracks, flaws or impurities;

2. The geometrical errors of the rectangular parallelepiped (parallelism of faces and perpendicularity of corners) must be low (<0.1%);

3. The starting guesses of elastic constants should be close to real values to avoid reaching a local minimum during the fitting process;

4. Measured resonances have to be assigned to the correct normal modes in the fit and any missed modes should be accounted for;

5. The number of missed modes should be less than 10% of the number of measured frequencies.

8.4. RUS apparatus

The most common method for detecting the mechanical resonant spectrum is illustrated in Figure 8.1, where a small parallelepiped-shaped sample is lightly held between two piezoelectric transducers. One transducer is used to generate an elastic wave of constant amplitude and varying frequency, whereas the other is used to detect the sample's resonance. As a frequency range is swept, a sequence of resonance peaks is recorded. The position of these peaks occurs at the natural frequencies f_n (from which the elastic constants are determined) and the quality factor Q (a measure of how narrow the resonance is) provides information about the dissipation of elastic energy. The presence of several transducers is needed to minimize the loading of the sample, in order to have the best possible match between the resonance frequencies and the natural ones. This results in a measurement accuracy on the order of 10%, whereas the measurement precision is always on the order of a few parts per million.

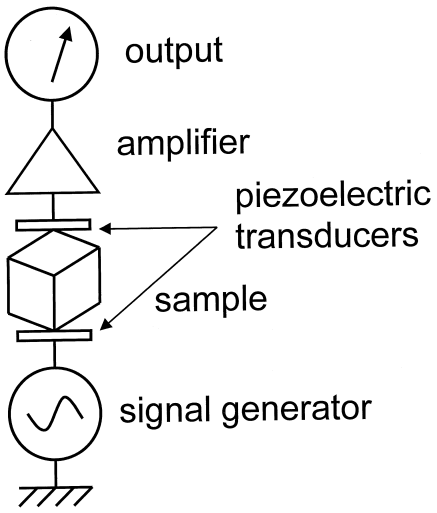

Fig. 8.1: Schematic of the two transducer resonant ultrasound spectroscopy set up (from Schwarz and Vuorinen, 2000).

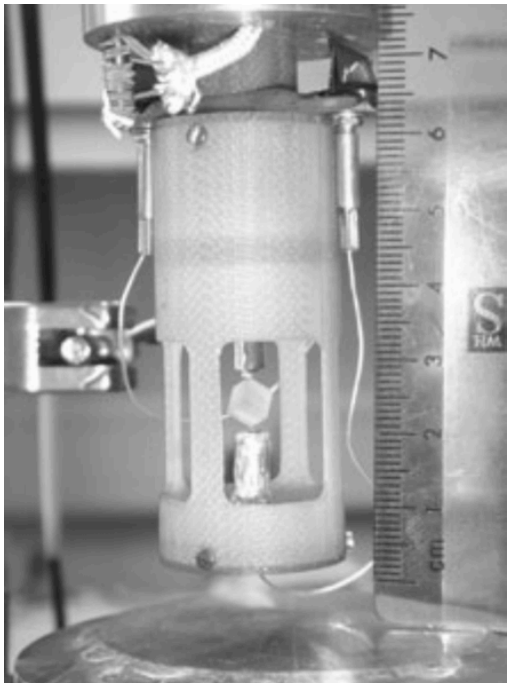

Fig. 8.2: The sample assembly for a RUS variable-temperature measurement (from Angel et al., 2009).

Unlike in a conventional ultrasonic measure, in a method that resonates the sample a strong coupling between the transducer and the sample is not required (see also § 8.4.4.), because the sample behaves as a natural amplifier. Rather, keeping at minimum the couple between them, you get a good approximation to free-surface boundary conditions and tend to preserve the *Q*, too.

For variable-temperature measurements the sample is held between the ends of two buffer rods that link the sample to the transducers (Fig. 8.2) because the transducers must be kept at room temperature. In terms of pressure, on the contrary, there is a limit of only a few bars, because the application of higher pressures leads to dampening of the resonances of the sample.

8.4.1. Room-temperature apparatus

The RUS stage for frequency measurements under ambient conditions is a very straightforward apparatus. The RUS head used for room-temperature measurements in this study is represented in Figure 8.3a, in which the parallelepiped (shown for perspective) is mounted on its opposite corners between two transducers, which are 2 mm in diameter. The transducers are coated in gold to reduce radio interference in the output signal, and are directly connected to the signal generator and detector electronics (Fig. 8.1). DRS M^3odulus II electronics are used to generate the signal and process the output spectrum.

8.4.2. Low-temperature apparatus

The low-temperature RUS apparatus consists of the standard RUS arrangement, with a rectangular parallelepiped mounted on opposite corners directly between the two 2 mm transducers, but the head has been modified for the cryostat. The RUS head itself is shown in Figure 8.3b.

The whole RUS head is attached to the end of a stick and inserted vertically into a standard *Orange 50 mm* helium flow cryostat, supplied by *AS Scientific Products Ltd* (Fig. 8.4a). After the RUS head, with the sample mounted, has been carefully lowered into the sample chamber, the chamber is sealed and vacuum pumped. Liquid nitrogen is added to achieve temperatures as low as 100 K. During this setup process, the sample chamber is held just below room temperature in order to avoid cooling the sample suddenly when cryogens are added to the system. Temperature regulation and measurement are achieved using a silicon diode and a LakeShore controller (Fig. 8.4b). At each stage in the process, RUS spectra are collected to check that the parallelepiped is still mounted correctly and sample resonance peaks are still detected. This is important as there is the possibility of the parallelepiped falling off the transducers at several points during the experimental setup because no bonding agent is used. A schematic diagram of a similar cryogenic RUS system to the one used here is shown in Figure 7.7 of Migliori and Sarrao (1997), who describe in detail the adaptations necessary to measure elastic behaviour at sub-ambient temperatures.

All materials for components used in the low-temperature system, including the wires connecting the RUS head to the computer, were specially selected so that they operated well down to temperatures as low as 5 K. Data can be collected during cooling and heating cycles at temperatures in the range of ~5–300 K with the temperature stability for each measurement being approximately ±0.1 K.

8.4.3. Samples

RUS can, in principle, be applied to a great range of samples sizes, with a minimum in the order or a few hundred microns with masses less than 100 μg,

and up to dimensions of several centimetres with masses of several kilograms, given the appropriate conditions (Maynard, 1996). However, for the measurement of mineral elasticity it is used on samples typically between 1 mm and 1 cm in size.

The sample, either a fully compressed polycrystalline aggregate or a single crystal, is machined in to a regular shape. Theoretically any sample shape can be used, but you obtain a substantial saving in computational time using rectangular parallelepiped resonators (RPR), spherical or cylindrical ones (less time savings with cylinders).

Since the accuracy of the measure depends strictly on the accuracy in the sample preparation, several precautions are taken: RPRs are prepared with the edges parallel to crystallographic directions; for cylinders only the axis can be matched to sample symmetry. RUS is rarely used for samples of lower symmetry, and for isotropic samples, alignment is irrelevant. For the higher symmetries, it is convenient to have different lengths edges to prevent a redundant resonance. Measurements on single crystals require orientation of the sample crystallographic axes with the edges of the RPR, to neglect the orientation computation and deal only with elastic moduli.

Polycrystalline samples should ideally be fully dense, free of cracks and without preferential orientation of the grains. Single crystal samples must be free of internal defects such as twin walls. The surfaces of all samples must be polished flat and opposite faces should be parallel. Once prepared, the density must be measured accurately as it scales the entire set of elastic moduli.

8.4.4. Transducers

Unlike all other ultrasonic techniques, RUS transducers are designed to make dry point contact with the sample. This is due to the requirement for free-surface boundary conditions (see § B.I.) for the computation of elastic moduli from frequencies. For RPRs this requires a very light touch between the sample's corners and the transducers. Corners are used because they provide elastically

weak coupling, reducing loading, and because they are never vibrational node points. Sufficiently weak contact ensures no transduced correction is required.

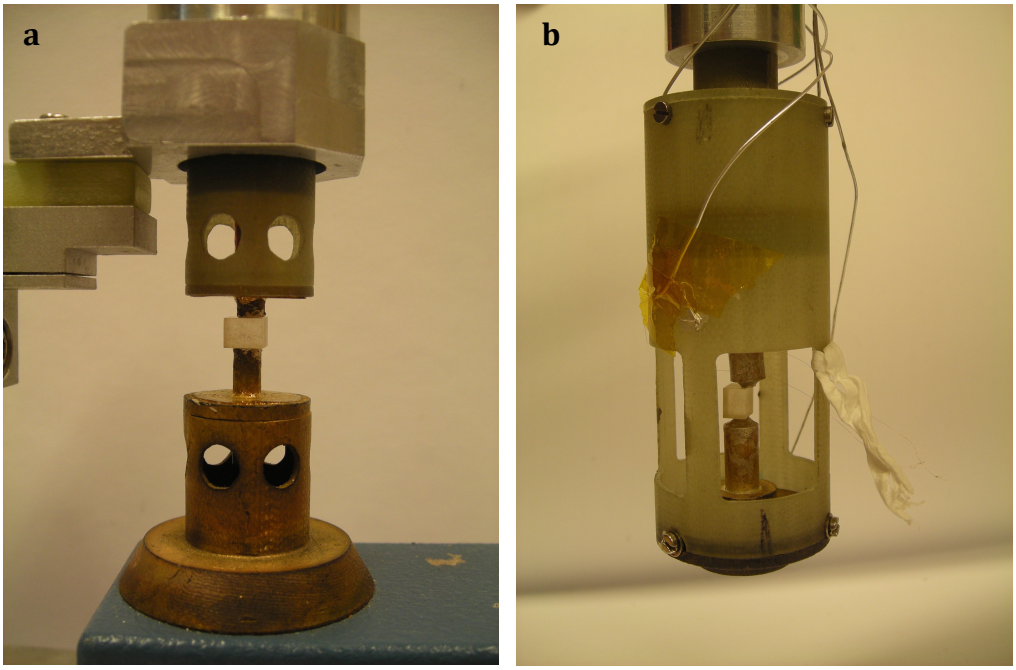

Fig. 8.3: A parallelepiped, with edge lengths of about 4 mm, is shown mounted on diametrically opposite corners for RUS experiments. (a) is the room-temperature stage; (b) is the head for low-temperature experiments, which is attached to the bottom end of a stick to be lowered into the cryostat. In all cases, the parallelepiped is held lightly between the two transducers without any bonding agent. The gold coating can be seen on the transducers.

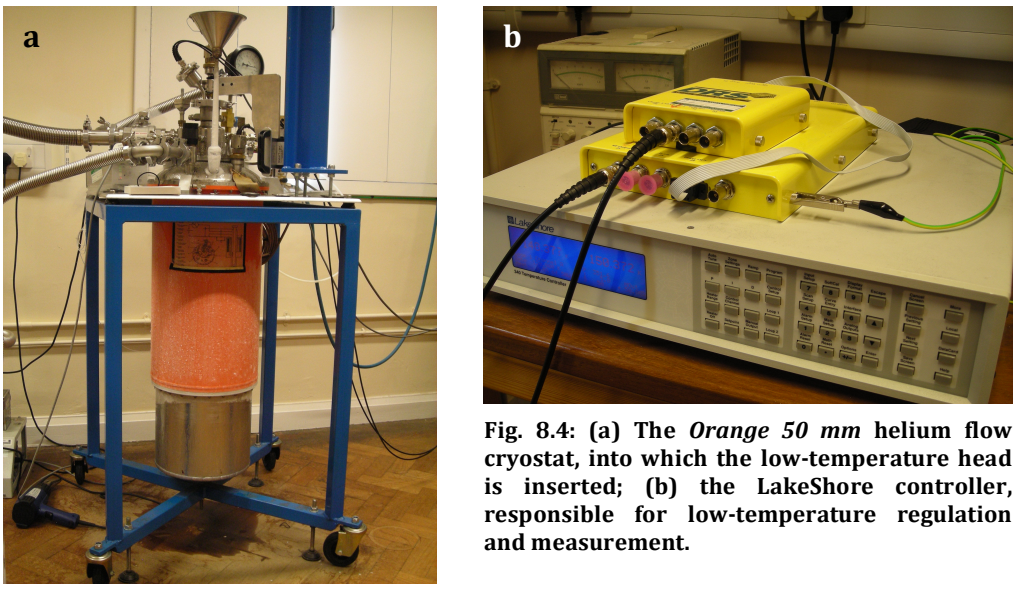

Fig. 8.4: (a) The *Orange 50 mm* helium flow cryostat, into which the low-temperature head is inserted; (b) the LakeShore controller, responsible for low-temperature regulation and measurement.

9. RUS data collection

The RUS data collection was carried out at the Department of Earth Sciences, University of Cambridge, from July the 8th to July the 13th 2014, under the supervision of Prof. Michael Carpenter, responsible for the RUS laboratory.

9.1. Sample description

The polycrystalline sample used for this study (reference number B803) was a cylinder cut out directly from a piston cylinder capsule (see Fig. 7.8a,b). PXRD analysis confirmed that it was made of pure coesite (see Fig. 7.7) and examination of SEM image showed that the sample had grain sizes approximately of 5 μm (see Fig. 7.10a) and no significant porosity. The cylinder was 1.091 mm in diameter and 0.541 mm in height. Its weight was 0.0010 g. Dimensions were measured using a standard digital micrometer. Mass was measured using an electronic analytical balance. From these values, density was calculated. Parallelism of opposite sides was assumed due to the careful sample preparation.

9.2. Room-temperature RUS experiments

The first step towards understanding the variation of elastic behaviour of any material with temperature is to understand its elastic properties at room temperature.

In order to carry out a full analysis at room temperature, all resonances of the sample should be observed and measured. For this reason, seven RUS spectra were collected (Fig. 10.1), with the sample mounted in different orientations for each spectrum (i.e. the sample was rotated or re-mounted on a different set of opposite corners). This ensures that no resonances are missed so that, during cooling experiments, it is known exactly how many resonances are expected to occur and approximately at what frequencies. The frequency range used was 50–1200 kHz, with 50000 data points. The TX gain, that is the voltage for amplification of the output signal, was left on the maximum setting (25 V). The

rest of the input parameters were left on the default settings: IF cycles = 1, no delay, IF code = 977 Hz. The number of IF cycles is the number of periods that the signal is averaged over, where a period is the length of time associated with the Intermediate Frequency (IF) which is specified by the IF code.

These preliminary spectra gave us peaks at frequencies higher than expected according to RPR fitting program, probably due to the imperfection of the sample. Since the cylinder was very small and soft, indeed, its surface could be rough and its shear modulus lower than found in literature (Weidner and Carleton, 1977).

On the basis of the above preliminary checks was therefore decided to extend the frequency range. The new frequency range was 50–3000 kHz, with 65000 data points. The TX gain was left always on the maximum setting (25 V), except for the last measurement, in which case the output spectrum showed very strong peaks and a lower setting had to be chosen (1 V). The rest of the input parameters were left on the default settings: IF cycles = 1, no delay, IF code = 977 Hz.

With this new parameters setting, the previous set of room-temperature measurements was updated with three new spectra (Fig. 10.2).

9.3. Low-temperature RUS experiments

Since coesite is not stable at high-temperature conditions, in order to avoid a back transformation to quartz during heating, only low-temperature experiments were performed. The sample was loaded into a cryostat RUS system, using liquid nitrogen as the cryogen so that temperatures as low as 100 K could be achieved.

After room-temperature measurements, the sample was thus mounted on the low-temperature RUS head for data collection below room temperature.

For low-temperature measurements on the polycrystalline cylinder, the system was cooled in 30 K intervals from 300 to 120 K with a 5 K temperature tolerance, and with a 20-minute equilibration time at each step. After each equilibration, a RUS spectrum was measured in the frequency range 300-2000 kHz with 65000 data points. The sample was then heated up again from 120 K to 300 K in 20 K steps, a 5 K tolerance, and a settle time of 20 minutes at each step. Spectra

collected at each step during heating were in the same frequency range and with the same number of data points as during the cooling cycle.

Spectra are usually collected at larger temperature intervals during cooling from room temperature, and then in smaller steps on heating back to room temperature simply to limit the use of expensive liquid nitrogen.

No temperature corrections were necessary for the low-temperature instrument, due to the carefully controlled sample environment. Based on well-known phase transitions, it is assumed that temperature readings from the LakeShore controller below room temperature are accurate to at least ±1 K.

9.4. Data analysis

The output spectrum from a RUS experiment is a plot of amplitude, in volts, as a function of frequency. The total amplitude is calculated from the *In phase* and *Quadrature* signals by Pythagoras' equation:

$$Amplitude = \sqrt{In\ phase^2 + Quadrature^2}. \qquad (9.1)$$

Peaks in the spectrum occur at the resonance frequencies of each of the normal modes in the sample. Absolute values of the amplitudes are variable as they depend on the mechanical coupling of the parallelepiped with the transducers, and therefore its orientation and positioning between them. The peak frequencies and their widths, however, are the quantities characteristic of any sample and, if measurable, provide detailed information about the elastic behaviour. Some peaks due to instrument noise may be present in the left part of the spectrum.

9.4.1. Frequency and Q^{-1} analysis

A set of resonance frequency values measured from a single RUS spectrum can be used to determine the elastic moduli of the sample, using a fitting procedure. Measurements of the full widths at half maximum (FWHM) may be used to determine the quality factor, Q, and therefore the mechanical dissipation for each resonance. In order to extract these values, all spectra collected using the DRS software were transferred to the software program *Igor Pro* (*Wavemetrics*). Each

individual peak was then modeled as an asymmetric Lorentzian function (Schreuer et al., 2003; Schreuer and Thybaut, 2005). The Lorentzian equation used for peak fits is

$$a(f) = a_0 + \frac{A}{(f-f_0)^2+B} \tag{9.2}$$

where *a(f)* is the amplitude; a_0 is the baseline; f_0 is the frequency at the peak maximum and therefore the frequency at which resonance occurs; and *A* and *B* are constants.

The peak fitting was carried out using the *Analysis* → *Curve fitting* feature of *Igor Pro* by inserting the text shown in Appendix C into the Procedure Window. Cursors were placed on either side of the peak to mark boundaries for the fit, and the *lorentz2* function, generated by the text in Appendix C, was selected for the fitting procedure. Input guesses for the coefficients in the *lorentz2* function are typically of the order of *w*_0 = *w*_5 = 0 (these two coefficients describe the baseline); *w*_1 = estimated frequency at the peak maximum and therefore the resonance frequency (in Hz); *w*_2, *w*_3, and w_4 describe the peak shape and are usually of the order of between 103 and 106. The output coefficient *w*_1 from the fit gives an exact value for the peak position and therefore the resonance frequency of that vibrational mode.

A plot of frequency values for a single resonance peak as a function of temperature provides a detailed view of how the elastic constants associated with that mode behave as a function of temperature, due to the fact that the elastic constant(s) associated with a resonance is/are directly proportional to the frequency squared, f_0^2, for any mode (Migliori and Sarrao, 1997).

Since absolute elastic moduli values can sometimes be hard to define due to the imperfection of the sample, that does not allow a successful RPR fitting procedure, the fact that elastic constants are directly related to frequency is very useful. The variation of resonant frequencies in a stacked plot of spectra as a function of temperature, in fact, directly tells us the variation of elastic moduli as they evolve with temperature as well.

The mechanical quality factor, *Q*, for any peak is given by

$$Q = \frac{f_0}{\Delta f}, \tag{9.3}$$

where f_0 is the peak frequency (as in equation 9.2) and Δf is the FWHM, obtained from the peak fitting process by inputting

```
print halfwidth (W_coef, x)
```

into the *Igor Pro* Command Window directly after a *lorentz2* fit has been carried out. The inverse quality factor, Q^{-1}, is a direct measure of acoustic dissipation within the sample. A plot of Q^{-1} as a function of temperature can therefore provide information on any relaxation mechanisms that may operate in the material. The limit of instrumental resolution for dissipation measurements it is assumed to be better than $Q^{-1} = 0.0002$.

10. RUS results

10.1. Room-temperature results

Room-temperature spectra for polycrystalline coesite (Figg. 10.1 and 10.2) show relatively weak, broad peaks.

The first sample resonances for this sample at room temperature are at ~200 kHz. The signal below 200 kHz is due to background instrument noise.

Several attempts were made to fit the peaks in order to calculate absolute bulk and shear moduli (K and G, respectively) using the DRS software and assuming an isotropic medium. Starting values for the fit were the Hill averages for K_T and G calculated by Weidner and Carleton (1977) (K_T = 113.7 GPa; G = 61.6 GPa). These failed to give an internally consistent fit to the peak frequencies, due both to the presence of cracks and to the fact that the sample was not totally porosity-free.

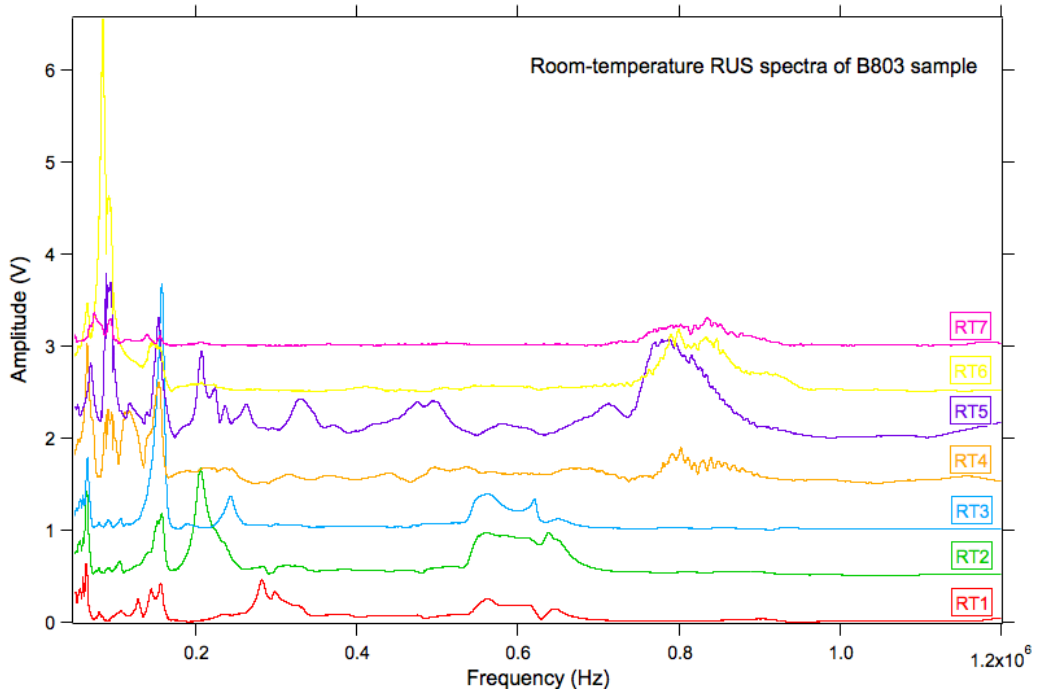

Fig. 10.1: Room-temperature RUS spectra showing resonances for polycrystalline coesite in the frequency range 50-1200 kHz. The seven separate spectra represent the cylinder mounted in seven different orientations so that as many resonances as possible are excited and observed. Spectra are offset along the *y*-axis by different amounts for ease of comparison. The signal below 200 kHz in all spectra is due to background instrument noise.

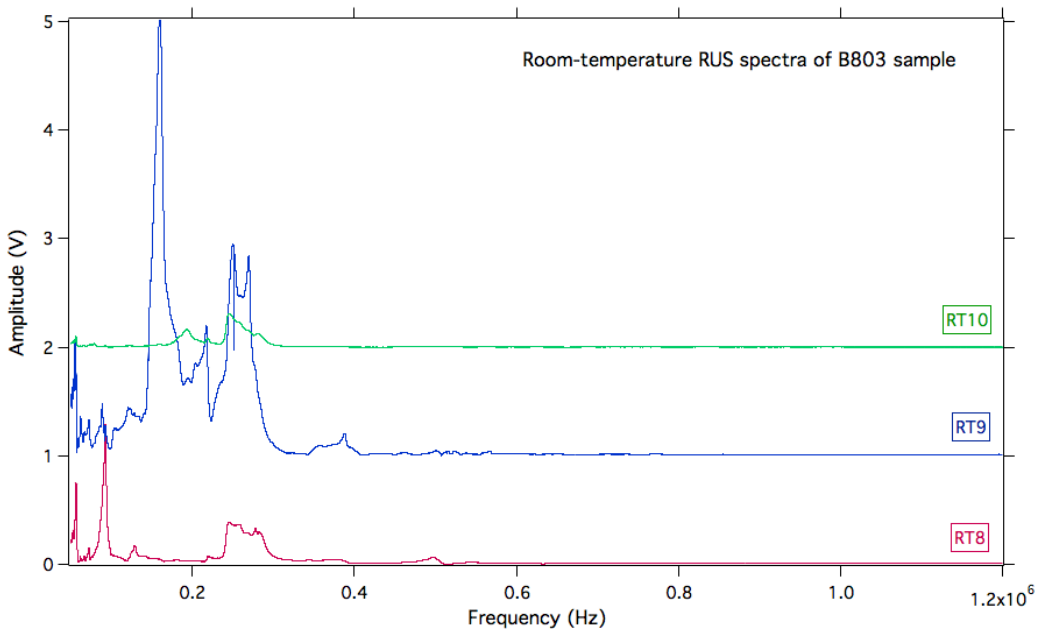

Fig. 10.2: Room-temperature RUS spectra showing resonances for polycrystalline coesite in the frequency range 50-3000 kHz. The three separate spectra represent the cylinder mounted in three different orientations so that as many resonances as possible are excited and observed. Spectra are offset along the *y*-axis by different amounts for ease of comparison. The signal below 200 kHz in all spectra is due to background instrument noise.

10.2. Low-temperature results

Figure 10.3 shows the RUS spectra for the polycrystalline coesite sample, which were collected as it was heated from 120 K to 300 K in 20 K intervals.

The *y*-axis of the data collected is amplitude (in volts) but each spectrum is offset from the *x*-axis by an amount proportional to the temperature at which it was collected to make it easy to visualize the way in which resonance peaks evolve across the temperature range. The spectrum collected at room temperature is at the top and the spectrum at the bottom is the lowest temperature measured (120 K).

As can be seen clearly from the stack, the frequencies of resonance peaks for polycrystalline coesite vary substantially (by up to 100 kHz) between 120 K and room temperature, and the variation is a linear function of temperature. On heating from 120 K, the resonances tend slightly and approximately constantly towards lower frequencies. There is a general trend of peak broadening on heating

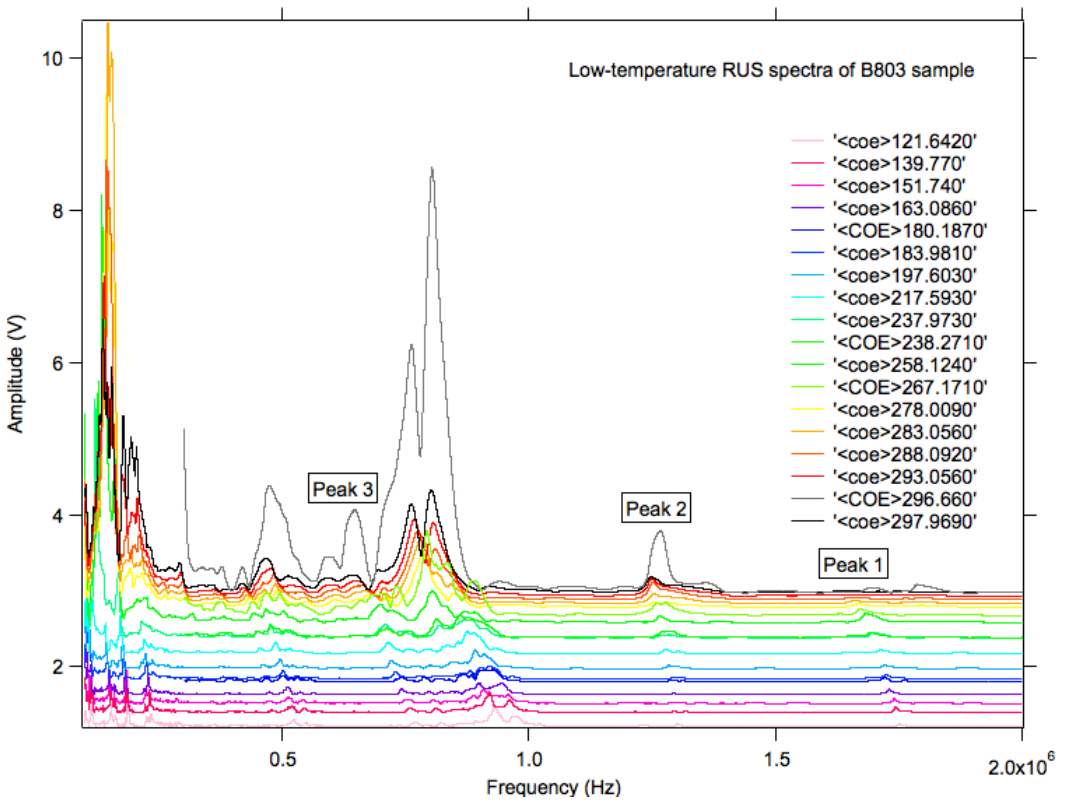

Fig. 10.3: RUS spectra for polycrystalline coesite in the frequency region 300–2000 kHz, collected at 20 K intervals on heating through the temperature range 120–300 K, stacked as a function of temperature. The spectrum at the top was collected at room temperature; the spectrum at the bottom was collected at the lowest temperature. The peaks labeled "Peak 1/2/3" are those on which the frequency and Q^{-1} analyses were performed.

across the whole temperature range, from sharper peaks at low temperatures to the broad, low Q, peaks that are seen at room temperature in Figures 10.1 and 10.2. The variation of the inverse of the quality factor, Q^{-1} (Figg. 10.4a,b,c) as a function of temperature, which represents the behaviour of dissipation, is relatively low in the low-temperature part of the diagram. There is then a change in slope around 270 kHz, showing some increase in dissipation on heating.

One of the most obvious features that can be seen from both the stack of spectra and from the variation of Q^{-1} with temperature (Figg. 10.3 and 10.4a,b,c) is that the broad room-temperature peaks sharpen slightly towards lower temperatures, implying an increase in the quality factor, Q, and therefore a decrease in dissipation at low temperatures. This trend is typical for materials because dissipation is mainly caused by atomic vibration, which is reduced at lower temperatures.

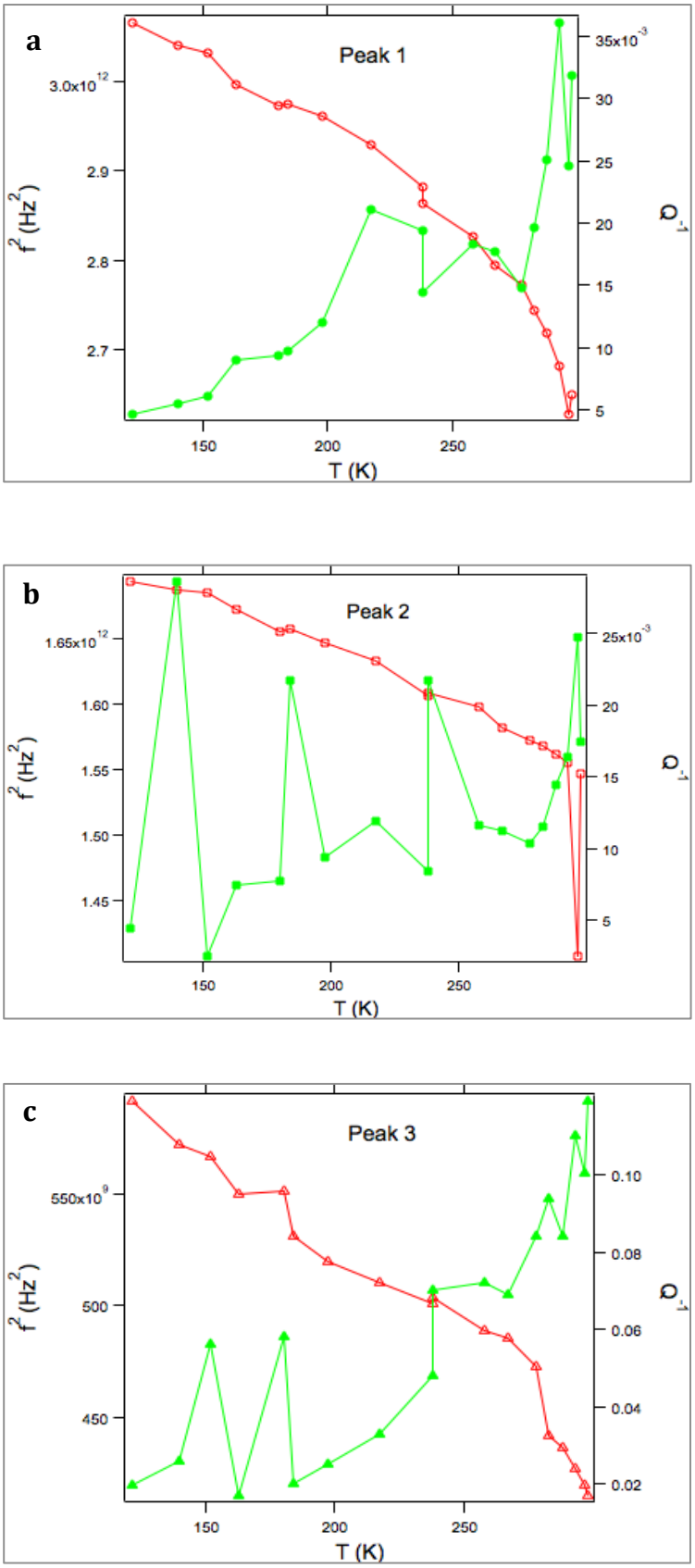

Fig. 10.4: Charts showing the variation of frequency squared (red) and of dissipation (green) as function of temperature for a) Peak 1, b) Peak 2 and c) Peak 3, previously indicated in Fig. 10.3. For all three peaks you can see a decrease of f^2 and an increase of Q^{-1} with heating.

Even though there is a decrease in dissipation toward lower temperatures, the value of Q^{-1} is relatively high in the whole temperature range. This is due to the presence of cracks that, expanding and contracting, make the resonance dispersed.

Another evident aspect from the above graphs is that the frequency squared increases with cooling. Considering the relationship between f_0^2 and the elastic constants (Migliori and Sarrao, 1997), this means that our sample becomes stiffer at low temperatures.

10.3. Elastic moduli

As already remarked, RUS is a technique capable to determine a complete set of elastic constants from one single measurement. Unfortunately, the extreme difficulty to produce a suitable polycrystalline sample of coesite made impossible to use successfully the RPR software. In detail, this software first solves the *forward* problem, and computes the expected resonance frequencies, given the input parameters (sample dimensions, weight and initial guesses for C_{11} and C_{44}). It then solves the *inverse* problem, by quantifying the difference between the calculated and measured resonance spectrum and minimizing the difference by varying the values of the elastic moduli, using a least squares fitting procedure.

Nevertheless, basing on the following considerations: (*i*) our spectra showed without any doubt some peaks coming from the sample; (*ii*) $f^2 \propto G$ (Migliori and Sarrao, 1997); (*iii*) all the resonance modes are a combination of both the elastic moduli, but, since the fraction of the pure shear is always preponderant, we could assume the trend of f^2 as the trend of G with temperature.

We therefore performed on all the three peaks indicated in Figure 10.3 the below reported calculation to infer the trend of K_S with temperature:

1) We obtained the absolute value of G for coesite from the K_S reported by Angel et al. (2001) by the calculation described in Appendix D;
2) We divided the room-temperature value of f^2 by G to find the coefficient of direct proportionality (k) that relates the two;

3) We applied k to the value of f^2 measured at the lowest temperature to find the relative G (G_{121});
4) We calculated K_s at the lowest temperature from G_{121};
5) We calculated the variation of K_s as a function of temperature ($\frac{\partial K_s}{\partial T}$).

Following these steps, the best $\frac{\partial K_s}{\partial T}$ obtained was - 0.041 GPa/K. This value stays in the typical order of magnitude known for this parameter (Levien and Prewitt, 1981), but is still not acceptable for coesite. In this case, in fact, diamonds would have grown and trapped their coesite inclusions in the stability field of graphite (see Chapter 14) and this is absolutely paradoxical from a mineralogical point of view.

11. First principles methods

Considering the non-completely comprehensive results of RUS analyses, a collaboration with Dr. Donato Belmonte (University of Genova) and Dr. Mauro Prencipe (University of Torino) was established with the aim to obtain the thermal expansion data on coesite by performing *ab initio* calculations. These data were needed to calculate the pressure of formation of coesite inclusions in diamonds and thus to valuate the reliability of the coesite-diamond geobarometer.

11.1. Introduction

The inner structure of the Earth and its dynamics are relatively well known at the global scale. The so-called shell structure (crust, mantle and nucleus) is part of a widely accepted model derived from a number of more or less direct sources of information: radius of the Planet; total mass; average density; abundances of chemical elements; isotopic abundances; minerals composing both the oceanic and the continental Earth crusts; xenoliths; the Earth's magnetic field; the presence and distribution of past and present dynamic phenomena. Other information can be derived from laboratory experiments, from petrological knowledge and thermodynamics.

A crucial role in the construction of a realistic model of the Earth is played by seismic tomography which is used either (*i*) to provide direct data concerning the presence of discontinuities at several depths along the Earth radius, together with the elastic properties of the different layers crossed by the seismic waves, or (*ii*) as a test of consistency of the structural model proposed for our Planet.

However, due to the complexity of the Earth's structure, the very interpretation of the data from the seismic technique is not possible without an *a priori* knowledge of a starting reasonably accurate model of the inner Earth. From this point of view, both the Earth's model and the base knowledge required to correctly interpret data from seismic tomography are self-consistently refined in a cycle where results from one step serve as an input to the subsequent one, whose output is reintroduced as input to the first step, until self-consistency is reached. A

central key of such cycle is the knowledge of the elastic properties, together with their temperature dependence, of materials supposed to be present at various depths.

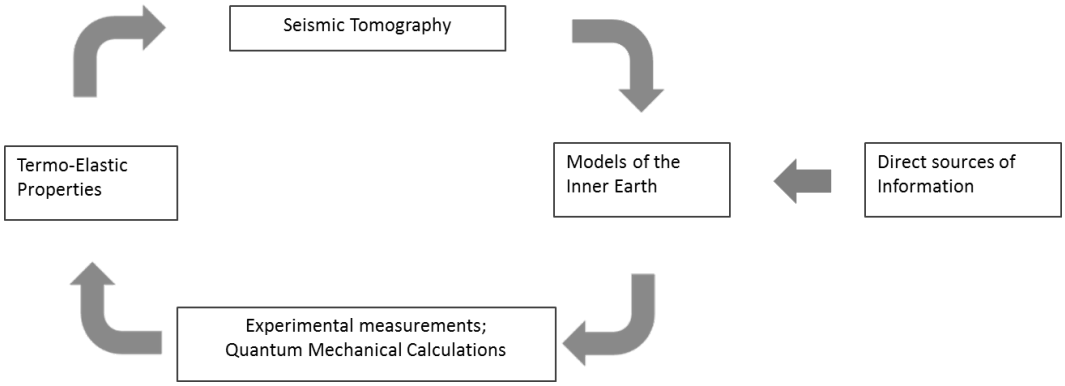

Fig. 11.1: Building a reliable model of the Earth with data from seismic tomography, *self-consistently* refined by using experimental determinations and quantum-mechanical calculations of the thermo-elastic properties of the material supposed to be present in the inner Earth.

Indeed, the relevant properties of crystals can in many instances be experimentally determined. However, technical difficulties may prevent the accurate measurements of the compressibility at simultaneous high pressure and temperature (HP/HT) conditions, which are typical of the Earth's mantle and core. In this case, HP/HT *first principles* (*ab initio*) simulations of structure and properties of crystals can provide an important support.

11.2. The ab initio approaches

As written above, one of the aim of *ab initio* calculations is to reproduce properties of crystals, at any P/T condition, with the least possible amount of *a priori* empirical information. In principle, no information other than the chemical composition of the material should be required; in practice, an approximated starting structure of the crystal (symmetry; approximated cell parameters and atomic fractional coordinates) is very often mandatory prior information for a successful simulation. The starting point of any quantum treatment of the solid state is the Schrödinger equation

$$H\Psi = E\Psi \qquad (11.1)$$

where H is the Hamiltonian operator, Ψ is the wave function, and E is the total energy of the unit cell of the crystal. The Hamiltonian operator specifies all of the possible energy contributions. The wave function does not have a direct physical meaning. The wave function squared, $|\Psi|^2 dV$, expresses conversely the probability that a given electron occupies a given volume element dV of space, that is the electron density.

11.2.1. The Hartree-Fock method

The Hartree-Fock (HF) method is a method of approximation for the determination of the wave function and the energy of a quantum many-body system in a stationary state. Basically it plans to approximate the ground-state wave function of the system by a specific Slater determinant, obtained by a variational method. This leads to a pseudo-Schrödinger equation, where the potential is function of the eigenfunctions themselves.

11.2.2. The Density Functional Theory

The Density Functional Theory (DFT) is one of the possible implementations of the theory and is based on the fundamental concept that it is possible to determine the energy of a system using only the electron density.

The ground-state energy, E_0, of a multielectronic system, in the presence of an external potential (the nuclei potential), is function of only the electronic density and can be obtained by integrating it.

By calculating partial derivatives of energy values it is possible to obtain observable physical quantities (e.g. bulk properties), and some of these quantities are useful to describe the structural, vibrational and elastic properties of a crystalline solid.

Since the DFT approach produces higher electro-electron energy contributions than in the case of HF, and the latter one lacks on the Coulombic correlation term, a very effective method to compensate these errors is to mix them in the so-called “hybrid HF/DFT method”.

12. Coesite thermal expansion data

Thermal expansion data reported in Table 12.1 have been evaluated by the previously described *ab initio* approach (see Chapter 11), by using hybrid HF/DFT functionals, at the Department of Earth, Environment and Life Sciences of University of Genova. Volume values at temperatures higher than ambient conditions were effectively calculated by this method; on the contrary, data in the range 10-200 K have been only extrapolated from the previous ones. This discrepancy leads to a thermal expansion curve hardly to fit at low temperatures, as we will see in detail in Chapter 14.

Thermal expansion data reported in Table 12.1 are plotted in Figure 12.1. It can be noticed that values above 150-200 K follow a linear trend. Conversely, values go to saturation in the low-temperature part of the curve.

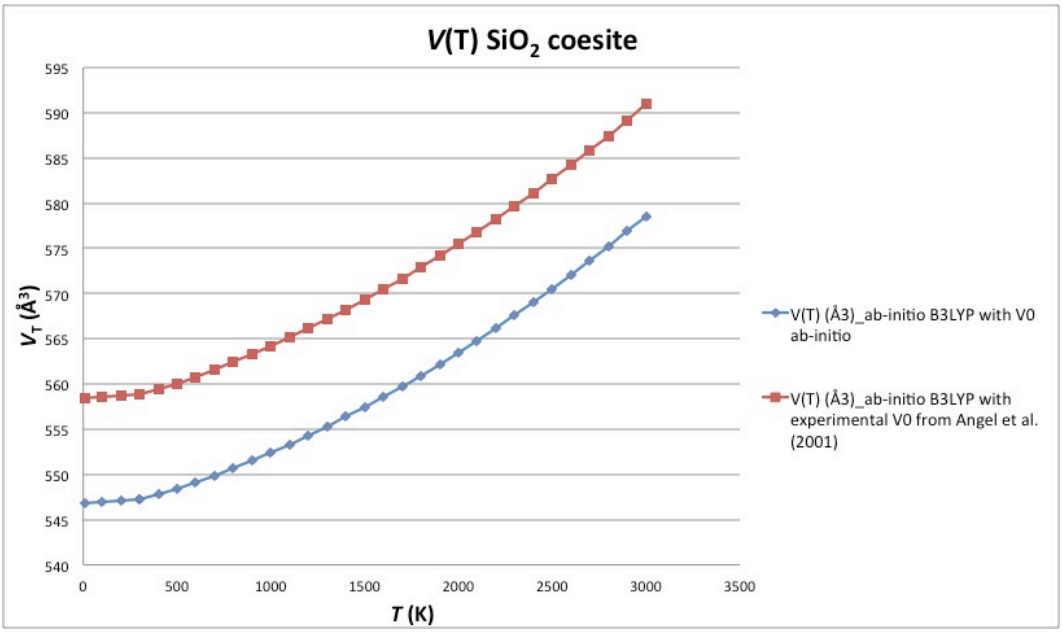

Fig. 12.1: Data reported in Table 12.1 are here plotted and the results are the thermal expansion curves for coesite in the temperature range 10-3000 K.

Tab. 12.1: Thermal expansion data on coesite evaluated by the hybrid B3LYP *ab initio* method.

T (K)	V(T) (Å^3)_ab-initio B3LYP with V_0 ab-initio	V(T) (Å^3)_ab-initio B3LYP with experimental V_0 from Angel et al. (2001)
10	558.4470415	546.7999864
100	558.5268158	546.8797607
200	558.7661389	547.0924923
298,15	558.9256876	547.252041
300	558.9256876	547.252041
400	559.4575166	547.7572786
500	560.0691199	548.3688819
600	560.7870891	549.0868511
700	561.5582411	549.8314117
800	562.3825761	550.6291552
900	563.2600939	551.4800816
1000	564.1642032	552.3841909
1100	565.1214954	553.3148916
1200	566.1053791	554.2721838
1300	567.1424456	555.2826589
1400	568.2061036	556.3463169
1500	569.3229445	557.4365664
1600	570.4663769	558.5534073
1700	571.6364007	559.7234311
1800	572.8861988	560.9200463
1900	574.135997	562.1698445
2000	575.4655695	563.4462341
2100	576.795142	564.7758066
2200	578.2044888	566.1319705
2300	579.6404271	567.5413174
2400	581.1029569	568.9772557
2500	582,645261	570,4663769
2600	584,1875651	572,008681
2700	585,8096435	573,5775765
2800	587,4583134	575,199655
2900	589,1601662	576,8749163
3000	590,9152019	578,5767691

13. Thermal expansion

13.1. Background

The volume thermal expansion of a material is defined as $\alpha(T) = V^{-1}(\partial V/\partial T)_P$. Integration of this expression yields the volume variation with temperature at constant pressure: $V_{0T} = V_{00} exp \int_{T_{ref}}^{T} \alpha(T)\, dT$, where T_{ref} is a reference temperature at which the volume is V_{00} (Angel et al., 2014c).

The only thermodynamic constraints on the form of the function for $\alpha(T)$ are that $\alpha(T) = \partial a/\partial T = 0$ at absolute zero. Consequently many different forms have been proposed in literature:

a) Berman. In 1988 Berman proposed a simple extension to accommodate non-linear thermal expansion:

$$V_{0T} = V_{00}\left(1 + \alpha_0\left(T - T_{ref}\right) + \tfrac{1}{2}\alpha_1\left(T - T_{ref}\right)^2\right).$$

Given the small changes in volume with temperature, differentiation is approximately $\alpha \approx \left[\alpha_0 + \alpha_1\left(T - T_{ref}\right)\right]$. The parameter α_0 is the thermal expansion coefficient at T_{ref}. However, this equation is not valid for low temperatures.

b) Fei. In 1995 Fei expanded the linear variation of thermal expansion to $\alpha = \alpha_0 + \alpha_1 T + \alpha_2 T^{-2}$. This leads to

$$V_{0T} = V_{00} exp\left(\alpha_0\left(T - T_{ref}\right) + \tfrac{1}{2}\alpha_1\left(T^2 - T_{ref}^2\right) - \alpha_2\left(\tfrac{1}{T} - \tfrac{1}{T_{ref}}\right)\right).$$

The advantages are, first, that α_0, α_1 and α_2 are values at 0 K so they are independent of T_{ref} and, secondly, that the differentiation is exactly $\alpha = \alpha_0 + \alpha_1 T + \alpha_2 T^{-2}$ at all temperatures. The disadvantage is that the full expression predicts non-physical behaviour at low temperatures.

c) Modified Holland & Powell (1998) equation. Pawley, Redfern and Holland (1996) proposed a model that ensures that the thermal expansion

becomes constant at high temperatures. Since this is sufficient only to model low-resolution datasets, their equation has been then improved (Angel et al., 2014c) to

$$V_{0T} = V_{00}\left(1 + \alpha_0\left(T - T_{ref}\right) - 2(10\alpha_0 + \alpha_1)\left(\sqrt{T} - \sqrt{T_{ref}}\right)\right).$$

The entire term $(10\alpha_0 + \alpha_1)$ of this equation is equal to the α_1 coefficient used by Pawley et al. (1996). Thus, when α_1 is fixed at zero the whole term $(10\alpha_0 + \alpha_1)$ becomes equal to $10\alpha_0$ and the equation proposed by Pawley et al. (1996) and used in Holland & Powell (1998) is obtained.
This equation cannot be used at low temperatures.

d) Salje. The equation of Salje, Wruck and Thomas (1991) has been re-written by Angel et al. (2014c) as

$$V_{0T} = \left[V_{00}^{1/3} + p_1\theta_{sat}[coth(\theta_{sat}/T) - 1]\right]^3$$

in order for the parameter V_{00} to have the value of the volume at the temperature $T_{ref} = 0\ K$. This equation can only be used to describe volume variation at low temperatures, because at moderate temperatures the thermal expansion becomes almost independent of temperature.

e) Kroll form of Holland & Powell (2011). As seen in the previous descriptions, it is hard to meet simultaneously the thermodynamic requirement $\alpha(T) = \partial a/\partial T = 0$ at $T = 0$ and match the experimental observation that $\alpha(T)$ becomes linear with temperature at high temperatures. For this reason, in 2012 Kroll et al. developed an equation for thermal expansion that explicitly relates the volume to lattice energy of the material:

$$V_{0T} = V_{00}\left(-K'_{00} + (1 + K'_{00})\left(1 - \frac{K'_{00}(K'_{00}+2)}{(K'_{00}+1)}A\right)^B\right).$$

Term A contains the Einstein temperature, θ_E, which can be approximated from the molar standard state entropy.

13.2. P-V-T equations of state

Equations to describe the variation of volume with both pressure and temperature can be developed by combining any thermal expansion model (see § 13.1.) with any isothermal equation of state (see Appendix A), and a model of the variation of bulk modulus with temperature at room pressure, $\partial K_{0T}/\partial T$.

14. Pressure of formation: EosFit software as a main calculation tool

EosFit is a program originally developed by Dr. Ross J. Angel (Angel, 2002) and recently updated with the collaboration of Dr. Javier Gonzalez-Platas and Dr. Matteo Alvaro (Angel et al., 2014c) to perform calculations involving both thermal expansion and equations of state. It is composed by two softwares: (1) EosFit7c, a console program that runs to manipulate EoS data, fit equations of state and thermal expansion, and to perform EoS calculations, but without graphics; (2) EosFit7 GUI, a full-GUI program that provides all of the tools needed to visualise and analyse the variations of unit-cell parameter and volume data with pressure and/or temperature.

In order to calculate the pressure of formation of diamond-coesite pairs following the method explained in Chapter 4, we proceed as follows:

1. We preliminarily inserted in EosFit7 GUI the dataset reported in Table 12.1 and we fitted the resulting thermal expansion curve to a Fei equation (see §

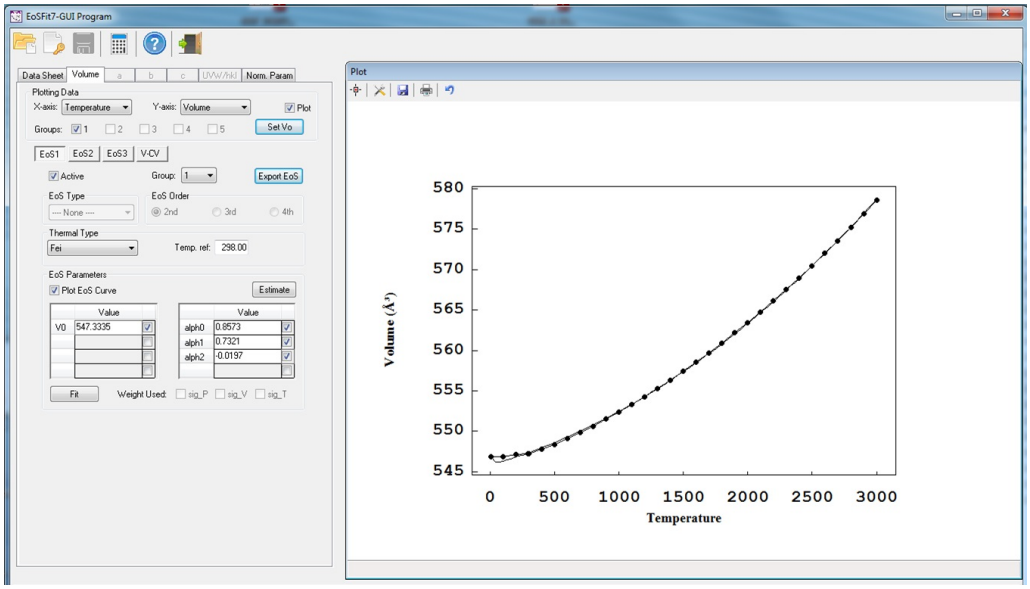

Fig. 14.1: Screenshot captured in EosFit7 GUI, showing the thermal expansion curve resulting from data reported in Table 12.1 and its fitting to a Fei equation. In the left bottom part of the diagram it can be seen the poor fitting of the curve at 10, 100 and 200 K.

13.1.). Since values in the range 10-200 K had not been calculated by *ab initio* method, but had been only extrapolated from the higher-temperature data, the fit was not reliable for the low-temperature part of the curve (Fig. 14.1). Thus, we decided to omit values in the range 10-200 K for the fitting of the thermal EoS.

2. In EosFit7c we fitted the *T-V* dataset by Belmonte (unpublished; see Tab. 12.1) to a Fei equation considering only values in the range 298-3000 K. Since parameters obtained by *ab initio* methods cannot have, due to their intrinsic "calculated" nature, an estimated standard deviation (esd), we decided to set it manually for all the volume data, just to "help" the software in performing the fitting. Basing on the average of the esd's measured experimentally by Angel et al. (2001) we decided to set the $\delta V = 0.03$ Å^3. The last refinement (Fig. 14.2) gave us the following parameters: $V_0 = 547.24(2)$ Å^3, $\alpha_0 = 1.04(1)$, $\alpha_1 = 0.645(6)$ and $\alpha_2 = -0.38(4)$:

```
  RESULTS AFTER FINAL REFINEMENT CYCLE
PARA REF          NEW            SHIFT           E.S.D.       SHIFT/ERROR
V0      1       547.23846          0.00004         0.02005          0.00
alph0   1         1.03720         -0.00002         0.01349         -0.00
alph1   1         0.64525          0.00001         0.00651          0.00
alph2   1        -0.37537          0.00001         0.04112          0.00
 REFERENCE TEMPERATURE = 298.00
W-CHI^2 =   0.18 (ESD'S NOT RESCALED)
```

Fig. 14.2: Screenshot captured in EosFit7c, showing the last refinement cycle for the *T-V* EoS for coesite.

3. We fitted the *P-V* dataset by Angel et al. (2001) to a fourth-order Birch-Murnaghan EoS (see Appendix A). The last refinement (Fig. 14.3) gave us the following parameters: $V_0 = 546.73(5)$ Å^3, $K_0 = 100.8(10)$ GPa, $K' = 1.8(6)$ and $K'' = 0.56(12)$.

```
  RESULTS AFTER FINAL REFINEMENT CYCLE
PARA REF          NEW            SHIFT           E.S.D.       SHIFT/ERROR
V0      1       546.73114          0.00009         0.04645          0.00
K0      1       100.80235         -0.00210         1.00267         -0.00
Kp      1         1.77263          0.00135         0.59037          0.00
Kpp     1         0.56048         -0.00027         0.12162         -0.00
W-CHI^2 =   5.51 (AND ESD'S RESCALED BY W-CHI^2)
```

Fig. 14.3: Screenshot captured in EosFit7c, showing the last refinement cycle for the *P-V* EoS for coesite.

4. We created three *P-V-T* EoS for coesite. Each of them resulted from the combination of the high-temperature EoS fitted in Step 2 and the high-pressure EoS fitted in Step 3, but they contained different values of $\partial K_{0T}/\partial T$. The first had a $\partial K_{0T}/\partial T = -0.021$ GPa/K (Levien and Prewitt, 1981), the second a $\partial K_{0T}/\partial T = -0.041$ GPa/K (calculated in this work; see § 10.3.) and the third a $\partial K_{0T}/\partial T = -0.0041$ GPa/K (an order of magnitude lower than the datum calculated in this work). This was done just to compare the results obtained using different $\partial K_{0T}/\partial T$, that is the hardest parameter to define experimentally.

5. Lastly, we performed the isomeke (see Chapter 4) calculation for all the three different *P-V-T* EoS of coesite described in the previous step. In order to do this, we had to insert both the *P-V-T* EoS of the diamond (host) and of the coesite (inclusion). The first one is given in Angel et al. (2014a) and is assumed to be corrected; the second is one of those created in Step 4.

   The isomeke calculation can be done either starting from the internal pressure of the inclusion (P_{inc}) or, vice versa, from the pressure of formation (P_E) of the host.

   In both the cases we assumed a relaxation model (see § 4.2.) for the host recently implemented in EosFit (Angel et al., 2014b).

   For the first calculation we started from some remnant pressures of coesite found in literature, that we consider reliable because they have been determined either by using high-pressure microRaman spectroscopy (Sobolev et al., 2000), whose database for coesite is well established, or by using single-crystal X-ray diffraction (Howell et al., 2012). In Table 14.1 the pressures of formation obtained by setting the temperature for the isomeke calculation at 1450 K, that is a reasonable value for the pressure of formation of diamonds, are reported.

Table 14.1: In this table the pressure of formation values for the diamond-inclusion pair resulting from the isomeke calculation described in Step 5 are reported in GPa. The reference temperature for the isomeke calculation is 1450 K, a reasonable value for the pressure of formation of diamonds.

$\partial K_{0T}/\partial T$ (GPa/K) / P_{inc} (GPa)	- 0.021 (Levien and Prewitt, 1981)	- 0.041 (Calculated in this work)	- 0.0041 (One order of magnitude lower than the value calculated in this work)
2.68 (Sobolev et al., 2000)	3.366	2.183	4.524
2.70 (Howell et al., 2012)	3.458	2.242	4.651
3.62 (Sobolev et al., 2000)	4.466	2.879	6.048

The unique value comparable with the pressure of formation of diamond provided by Sobolev et al. (2000) (5.5 ± 0.5 GPa) is 6.048 GPa, calculated adopting a $\partial K_{0T}/\partial T = -0.0041$ GPa/K and a $P_{inc} = 3.62$ GPa, that is the highest value of remnant pressure for coesite ever reported in literature (Sobolev et al., 2000).

Moreover, as you can see from Figure 14.4, where we plotted data from Table 14.1, the above-mentioned datum of pressure of entrapment is the only one falling in the stability field of diamond.

Starting, instead, from the pressure of formation of the host fixed at 5.5 GPa, that is again the value reported by Sobolev et al. (2000), and setting the temperature for the isomeke calculation at 1450 K, we obtained the inclusion pressure values reported in Table 14.2.

Table 14.2: In this table the inclusion pressure values for the diamond-inclusion pair resulting from the isomeke calculation described in Step 5 are reported in GPa. The reference temperature for the isomeke calculation is 1450 K, a reasonable value for the pressure of formation of diamonds.

$\partial K_{0T}/\partial T$ (GPa/K) / P_E (GPa)	- 0.021 (Levien and Prewitt, 1981)	- 0.041 (Calculated in this work)	- 0.0041 (One order of magnitude lower than the value calculated in this work)
5.5 (Sobolev et al., 2000)	4.468	6.939	3.289

Also in this case it can be noticed that only making use of the value $\partial K_{0T}/\partial T = -0.0041$ GPa/K there is a correspondence between the entrapment pressure (5.5 ± 0.5 GPa GPa) and the inclusion pressure (3.62 GPa) indicated by Sobolev et al. (2000).

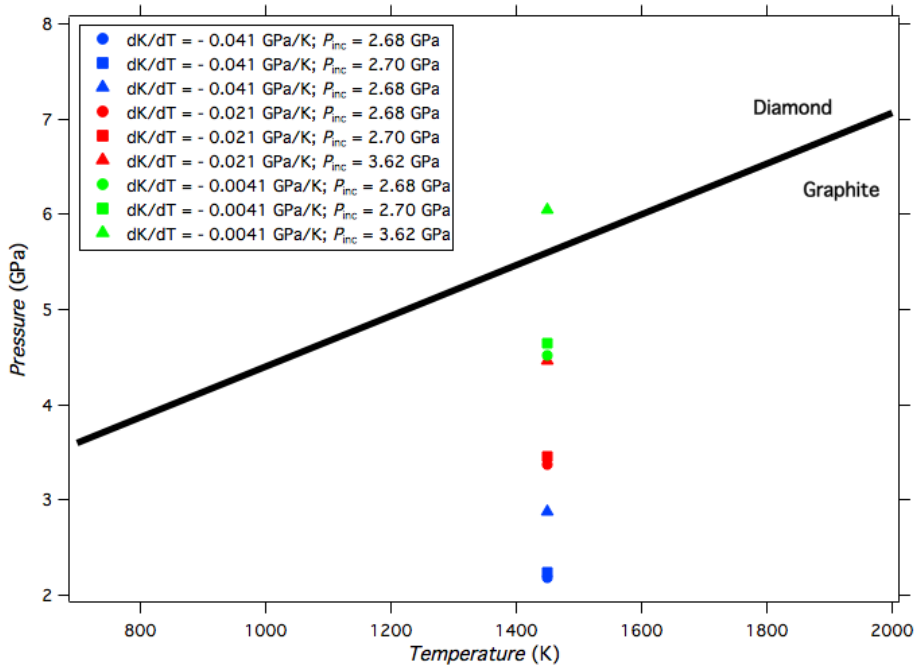

Fig. 14.4: In this figure the entrapment pressures reported in Table 14.1 are plotted. As you can easily see, the only datum that falls in the stability field of diamond and, consequently, the only value sensible from a mineralogical view is 6.048 GPa, marked with a green triangle. The graphite-diamond transition is estimated basing on the average of data from Getting and Kennedy (1970), Kennedy and Kennedy (1976).

Figure 14.4, where we plotted data from Table 14.1, clearly shows that all the values of entrapment pressure calculated using the inclusion pressure values found in literature (Sobolev et al., 2000; Howell et al., 2012) and a $\partial K_{0T}/\partial T = -0.021$ GPa/K (Levien and Prewitt, 1981) fall out of the stability field of diamond (red makers).

It also shows that the values of entrapment pressure calculated using the same inclusion pressure values and a $\partial K_{0T}/\partial T = -0.041$ GPa/K (determined in this work, see § 10.3.) fall in the stability field of graphite, too (blue markers).

The only pressure of formation value that falls above the graphite-diamond transition and is thus sensible from a mineralogical point of view is 6.048 GPa (marked with a green triangle). This value was calculated using a $\partial K_{0T}/\partial T = -0.0041$ GPa/K (one order of magnitude lower than the value determined in this work) and the highest remnant pressure value reported in literature (3.62 GPa).

The crux of the matter is that, assuming the thermal expansion is correct, the dependence of bulk modulus with temperature is certainly a parameter that needs to be revisited, because these two are the only two parameters affecting the calculation.

15. Conclusions

As we have seen in the first chapter, coesite has long been considered (at least in the past 15 years) one of the most important minerals in terms of geobarometry application to diamond science. The coesite-in-diamond pair, indeed, has many unique advantages (Sobolev et al., 2000). The high compressibility and low thermal expansivity of coesite provide the opportunity to preserve the maximum pressure with little dependence on the trapping temperature. The extremely simplified composition of coesite, furthermore, avoids the problems of chemical variability met in several other minerals found as inclusion in diamonds, which always make more complex their study.

Despite its strategic role in geobarometry, however, there still seem to be some gaps in our knowledge of coesite's elastic behaviour at high-temperature and high-pressure conditions.

I found, in fact, that if we apply the improved elastic method (Angel et al., 2014a) to the entrapment pressure provided by Sobolev et al. (2000) (5.5 ± 0.5 GPa GPa), adopting the same $\partial K_{0T}/\partial T$ (- 0.021 GPa/K) used in that work, even the highest inclusion pressure stated by the authors (3.62 GPa) appears to be underestimated compared to our result (4.468 GPa, see Table 14.2).

I also found that, if we apply the same method to the more recent inclusion pressures available in literature for coesite (Sobolev et al., 2000; Howell et al., 2012), the unique value of entrapment pressure falling in the stability field of diamond arises by adopting a temperature dependency bulk modulus one order of magnitude lower than the typical $\partial K_{0T}/\partial T$ known for minerals (that usually stays in the range from - 0.01 to - 0.03 GPa/K, e.g. Mao et al., 2011; Yang et al., 2014).

The possible explanations for this discrepancy are:

1. Diamonds do not form in their stability field;
2. The thermal expansion of coesite (Fei et al., 1990) is wrong; including the one calculated by *ab initio* methods in this work (see Chapter 12);
3. The $\partial K_{0T}/\partial T$ is abnormally low in the case of coesite, even one order

of magnitude lower than the typical temperature derivative values known for minerals.

4. The elastic method performed via the isomeke calculation is not applicable when the thermal expansion of the inclusion is small (Bourova et al., 2004) and comparable to that of the host (Sobolev et al., 2000).

Considering that:

- ☒ The first hypothesis can be accounted as impossible from both a physical and a mineralogical point of view;
- ☒ The second and the third hypotheses can be considered at least unlikely, due to the efficacy demonstrated in obtaining such values for other minerals;
- ☑ The unique hypothesis considered conceivable is the fourth one.

The elastic method and the isomeke calculation are, after all, methods only recently improved and implemented in EosFit7c. There could therefore be some drawbacks and limitations, like the contrast thermo-elastic behaviour between the host and the inclusion, still unknown that can limit their efficacy.

Whether or not this is true, at the moment the coesite-diamond pair, reputed an excellent candidate for geobarometry due to its peculiarities, cannot be considered exploitable yet.

This work aims thus to be a starting point for a more-in-depth study not only on the thermoelastic parameters of coesite, but also on the range of use of the elastic method, together with the isomeke calculation.

References

Angel R.J., Alvaro M., Nestola F. and Mazzucchelli M.L., (2014a) Diamond thermo-elastic properties and implications for determining the pressure of formation of diamond-inclusion systems. Russian Geology and Geophysics, in press.

Angel R.J., Mazzucchelli M.L., Alvaro M., Nimis P., Nestola F. (2014b) Geobarometry from host-inclusion systems: the role of elastic relaxation. American Mineralogist, in press.

Angel, R. (2002) EOSFIT V5. 2. Crystallography Laboratory. Department of Geological Sciences Virginia Techology, USA.

Angel, R., Mosenfelder, J. and Shaw, C. (2001) Anomalous compression and equation of state of coesite. Physics of the Earth and Planetary Interiors, 124, 1, 71-79.

Angel, R.J., Alvaro, M. and Gonzalez-Platas, J. (2014c) EosFit7c and a Fortran module (library) for equation of state calculations. Zeitschrift für Kristallographie-Crystalline Materials, 229, 5, 405-419.

Angel, R.J., Jackson, J.M., Reichmann, H.J. and Speziale, S. (2009) Elasticity measurements on minerals: a review. European Journal of Mineralogy, 21, 3, 525-550.

Barron, L., Mernagh, T. and Barron, B. (2008) Using strain birefringence in diamond to estimate the remnant pressure on an inclusion. Australian Journal of Earth Sciences, 55, 2, 159-165.

Berman, R.G. (1988) Internally-consistent thermodynamic data for minerals in the system Na_2O-K_2O-CaO-MgO-FeO-Fe_2O_3-Al_2O_3-SiO_2-TiO_2-H_2O-CO_2. Journal of Petrology, 29, 2, 445-522.

Birch, F. (1947) Finite elastic strain of cubic crystals. Physical Review, 71, 11, 809.

Bohlen, S.R. and Boettcher, A. (1982) The quartz⇆ coesite transformation: a precise determination and the effects of other components. Journal of Geophysical Research: Solid Earth (1978–2012), 87, B8, 7073-7078.

Bose, K. and Ganguly, J. (1995) Quartz-coesite transition revisited: Reversed experimental determination at 500-1200° C and retrieved thermochemical properties. American Mineralogist, 80, 231-231.

Bourova, E., Richet, P. and Parker, S. (2004) High-temperature structure and dynamics of coesite (SiO_2) from numerical simulations. Physics and chemistry of minerals, 31, 9, 569-579.

Boyd, F. and England, J. (1960) Apparatus for phase-equilibrium measurements at pressures up to 50 kilobars and temperatures up to 1750° C. Journal of Geophysical Research, 65, 2, 741-748.

Chao, E.C., Shoemaker, E.M. and Madsen, B.M. (1960) First Natural Occurrence of Coesite. Science (New York, N.Y.), 132, 3421, 220-222.

Chesnokov, B. and Popov, V. (1965) Increase in the volume of quartz grains in South Urals eclogite. Dokl Akad Nauk SSSR, 162, 176-178.

Chopin, C. (1984) Coesite and pure pyrope in high-grade blueschists of the Western Alps: a first record and some consequences. Contributions to Mineralogy and Petrology, 86, 2, 107-118.

Coes, L., Jr (1962) Synthesis of minerals at high pressures. Modern very high pressure techniques, 137-150.

Coes, L., Jr (1953) A New Dense Crystalline Silica. Science (New York, N.Y.), 118, 3057, 131-132.

Day, H.W. (2012) A revised diamond-graphite transition curve. American Mineralogist, 97, 1, 52-62.

Demarest Jr, H.H. (1971) Cube-Resonance Method to Determine the Elastic Constants of Solids. The Journal of the Acoustical Society of America, 49, 3B, 768-775.

Dunn, T. (1993) The piston-cylinder apparatus. Mineralogical Association of Canada, Short Course Handbook, 21, 39-94.

Fei, Y. (1995) Thermal Expansion. Mineral Physics & Crystallography: A Handbook of Physical Constants, 29-44.

Fei, Y., Saxena, S.K. and Navrotsky, A. (1990) Internally consistent thermodynamic data and equilibrium phase relations for compounds in the system MgO-SiO_2 at high pressure and high temperature. Journal of Geophysical Research: Solid Earth (1978–2012), 95, B5, 6915-6928.

Fraser, D. and LeCraw, R. (1964) Novel method of measuring elastic and anelastic properties of solids. Review of Scientific Instruments, 35, 9, 1113-1115.

Getting, I. and Kennedy, G. (1970) Effect of Pressure on the emf of Chromel-Alumel and Platinum-Platinum 10% Rhodium Thermocouples. Journal of Applied Physics, 41, 11, 4552-4562.

Gwanmesia, G.D., Li, B. and Liebermann, R.C. (1993) Hot pressing of polycrystals of high-pressure phases of mantle minerals in multi-anvil apparatus. Pure and Applied Geophysics, 141, 467-484.

Gwanmesia, G.D., Liebermann, R.C. and Guyot, F. (1990) Hot-pressing and characterization of polycrystals of β-$Mg2SiO_4$, for acoustic velocity measurements. Geophysical Research Letters, 17, 9, 1331-1334.

Gwanmesia, G. and Liebermann, R. (1992) Polycrystals of high-pressure phases of mantle minerals: Hot-pressing and characterization of physical properties. Geophysical Monograph Series, 67, 117-135.

Hacker, B.R. and Abers, G.A. (2012) Subduction Factory 5: Unusually low Poisson's ratios in subduction zones from elastic anisotropy of peridotite. Journal of Geophysical Research: Solid Earth (1978–2012), 117, B6.

Harris, J. (1968) Recognition of Diamond Inclusions. 1. Syngenetic Mineral Inclusions. Industrial Diamond Review, 28, 334, 402-410.

Hemingway, B.S., Bohlen, S.R., Hankins, W., Westrum, E.F. and Kuskov, O.L. (1998) Heat capacity and thermodynamic properties for coesite and jadeite, reexamination of the quartz-coesite equilibrium boundary. American Mineralogist, 83, 5, 409-418.

Hemley, R. (1987) Pressure Dependence of Raman Spectra of SiO_2 Polymorphs: α-Quartz, Coesite, and Stishovite. High-Pressure Research in Mineral Physics: A Volume in Honor of Syun-iti Akimoto, 347-359.

Holland, T. and Powell, R. (2011) An improved and extended internally consistent thermodynamic dataset for phases of petrological interest, involving a new equation of state for solids. Journal of Metamorphic Geology, 29, 3, 333-383.

Holland, T. and Powell, R. (1998) An internally consistent thermodynamic data set for phases of petrological interest. Journal of Metamorphic Geology, 16, 3, 309-343.

Hollemann, A. and Wiberg, N. (1985) Lehrbuch der Anorganischen Chemie (91^{st}–100^{th} edition) Walter de Gruyter. New York, Berlin.

Howell, D., Wood, I., Dobson, D., Jones, A., Nasdala, L. and Harris, J. (2010) Quantifying strain birefringence halos around inclusions in diamond. Contributions to mineralogy and petrology, 160, 5, 705-717.

Howell, D., Wood, I.G., Nestola, F., Nimis, P. and Nasdala, L. (2012) Inclusions under remnant pressure in diamond: a multi-technique approach. European Journal of Mineralogy, 24, 4, 563-573.

Huang, Y. and Chow, C. (1974) The generalized compressibility equation of Tait for dense matter. Journal of Physics D: Applied Physics, 7, 15, 2021.

Ikuta, D., Kawame, N., Banno, S., Hirajima, T., Ito, K., Rakovan, J.F., Downs, R.T. and Tamada, O. (2007) First in situ X-ray identification of coesite and

retrograde quartz on a glass thin section of an ultrahigh-pressure metamorphic rock and their crystal structure details. American Mineralogist, 92, 1, 57-63.

Izraeli, E., Harris, J. and Navon, O. (1999) Raman barometry of diamond formation. Earth and Planetary Science Letters, 173, 3, 351-360.

Kennedy, C.S. and Kennedy, G.C. (1976) The equilibrium boundary between graphite and diamond. Journal of Geophysical Research, 81, 14, 2467-2470.

Kroll, H., Kirfel, A., Heinemann, R. and Barbier, B. (2012) Volume thermal expansion and related thermophysical parameters in the Mg, Fe olivine solid-solution series. European Journal of Mineralogy, 24, 6, 935-956.

Levien, L. and Prewitt, C.T. (1981) High-pressure crystal structure and compressibility of coesite. American Mineralogist, 66, 3-4, 324-333.

Li, B., Rigden, S.M. and Liebermann, R.C. (1992) Pressure derivatives of the elastic wave velocities in polycrystalline stishovite. EOS Trans. AGU, 73.

Li, B., Rigden, S.M. and Liebermann, R.C. (1996) Elasticity of stishovite at high pressure. Physics of the Earth and Planetary Interiors, 96, 2, 113-127.

Li, G. and Gladden, J. (2011) High Temperature Resonant Ultrasound Spectroscopy: A Review. International Journal of Spectroscopy.

Mao, Z., Lin, J., Liu, J. and Prakapenka, V.B. (2011) Thermal equation of state of lower-mantle ferropericlase across the spin crossover. Geophysical Research Letters, 38, 23.

Maynard, J. (1996) Resonant ultrasound spectroscopy. Physics Today, 49, 26-31.

Migliori, A., Darling, T., Baiardo, J. and Freibert, F. (2001) 5. Resonant ultrasound spectroscopy (RUS). Experimental Methods in the Physical Sciences, 39, 189-220.

Migliori, A. and Sarrao, J.L. (1997) Resonant ultrasound spectroscopy: applications to physics, materials measurements, and nondestructive evaluation Wiley New York.

Mosenfelder, J. (2000) Pressure dependence of hydroxyl solubility in coesite. Physics and Chemistry of Minerals, 27, 9, 610-617.

Murnaghan, F.D. (1937) Finite deformations of an elastic solid. American Journal of Mathematics, 235-260.

Nasdala, L., Brenker, F.E., Glinnemann, J., Hofmeister, W., Gasparik, T., Harris, J.W., Stachel, T. and Reese, I. (2003) Spectroscopic 2D-tomography Residual pressure and strain around mineral inclusions in diamonds. European journal of mineralogy, 15, 6, 931-935.

Nestola, F., Nimis, P., Ziberna, L., Longo, M., Marzoli, A., Harris, J.W., Manghnani, M.H. and Fedortchouk, Y. (2011) First crystal-structure determination of olivine in diamond: Composition and implications for provenance in the Earth's mantle. Earth and Planetary Science Letters, 305, 1, 249-255.

Nestola, F., Merli, M., Nimis, P., Parisatto, M., Kopylova, M., De Stefano, A., Longo, M., Ziberna, L. and Manghnani, M. (2012) In situ analysis of garnet inclusion in diamond using single-crystal X-ray diffraction and X-ray micro-tomography. European Journal of Mineralogy, 24, 4, 599-606.

Ohno, I. (1976) Free vibration of a rectangular parallelepiped crystal and its application to determination of elastic constants of orthorhombic crystals. Journal of Physics of the Earth, 24, 4, 355-379.

Pawley, A., Redfern, S.A. and Holland, T. (1996) Volume behavior of hydrous minerals at high pressure and temperature: I. Thermal expansion of lawsonite, zoisite, clinozoisite, and diaspore. American Mineralogist, 81, 3, 335-340.

Perrillat, J., Daniel, I., Lardeaux, J. and Cardon, H. (2003) Kinetics of the coesite–quartz transition: application to the exhumation of ultrahigh-pressure rocks. Journal of Petrology, 44, 4, 773-788.

Poirier, J. and Tarantola, A. (1998) A logarithmic equation of state. Physics of the Earth and Planetary Interiors, 109, 1, 1-8.

Ponomarenko, A., Spetsius, Z. and Lyubushkin, V. (1977) Kyanite eclogite with coesite. Dokl Akad Nauk SSSR, 236, 215-219.

Rykart, R. (1995) Quarz-Monographie: die Eigenheiten von Bergkristall, Rauchquarz, Amethyst, Chalcedon, Achat, Opal und anderen Varietäten Ott.

Salje, E., Wruck, B. and Thomas, H. (1991) Order-parameter saturation and low-temperature extension of Landau theory. Zeitschrift für Physik B Condensed Matter, 82, 3, 399-404.

Schreuer, J. and Thybaut, C. (2005) Anelastic relaxation effects and elastic instabilities in CGG-type compounds. In Ultrasonics Symposium, 2005 IEEE, 1, 695-698.

Schreuer, J., Thybaut, C., Prestat, M., Stade, J. and Haussuhl, E. (2003) Towards an understanding of the anomalous electromechanical behaviour of langasite and related compounds at high temperatures. In Ultrasonics Symposium, 2003 IEEE, 1, 196-199.

Schwarz, R. and Vuorinen, J. (2000) Resonant ultrasound spectroscopy: applications, current status and limitations. Journal of Alloys and Compounds, 310, 1, 243-250.

Smith, D.C. (1984) Coesite in clinopyroxene in the Caledonides and its implications for geodynamics.

Smyth, J.R. and Hatton, C. (1977) A coesite-sanidine grospydite from the Roberts Victor kimberlite. Earth and Planetary Science Letters, 34, 2, 284-290.

Sobolev, N.V., Yefimova, E., Koptil, V. and Lavrent'yev, Y. Sobolev V. (1976): Inclusions of coesite, garnet and omphacite in diamonds of Yakutia-first find of coesite paragenesis. In Trans. Dokl. USSR Acad. Sci. Earth Sci. Sec, 230, 1443-1444.

Sobolev, N.V., Fursenko, B.A., Goryainov, S.V., Shu, J., Hemley, R.J., Mao, A. and Boyd, F.R. (2000) Fossilized high pressure from the Earth's deep interior: the coesite-in-diamond barometer. Proceedings of the National Academy of Sciences of the United States of America, 97, 22, 11875-11879.

Stachel, T. and Harris, J. (2008) The origin of cratonic diamonds—constraints from mineral inclusions. Ore Geology Reviews, 34, 1, 5-32.

Vinet, P., Ferrante, J., Rose, J. and Smith, J. (1987) Compressibility of solids. Journal of Geophysical Research: Solid Earth (1978–2012), 92, B9, 9319-9325.

Weidner, D.J. and Carleton, H.R. (1977) Elasticity of coesite. Journal of Geophysical Research, 82, 8, 1334-1346.

Wenk, H. and Bulakh, A. (2004) Minerals: their constitution and origin Cambridge University Press.

Yang, C., Inoue, T., Yamada, A., Kikegawa, T. and Ando, J. (2014) Equation of state and phase transition of antigorite under high pressure and high temperature. Physics of the Earth and Planetary Interiors, 228, 56-62.

Zhang, Y. (1998) Mechanical and phase equilibria in inclusion-host systems. Earth and Planetary Science Letters, 157, 3-4, 209-222.

Acknowledgments

Due anni fa ero stata sintetica, in linea con la tesi triennale. Stavolta, invece, a simbolizzare metaforicamente la "passione" di questi sudati 40 CFU, mi dilungherò nel ringraziare tutti quelli che, in un modo o nell'altro, mi hanno accompagnato fino all'ambito traguardo.

Prima di tutti vorrei ringraziare immensamente Fabrizio, per avermi offerto l'opportunità di lavorare su questo progetto, esaudendo il mio desiderio di svolgere una tesi di respiro "internazionale", e per aver mantenuto la promessa fino in fondo. Grazie per aver trovato il tempo di seguirmi con dedizione nonostante i tuoi mille impegni, per avermi dato asilo sia nei momenti di diletto che in quelli di pura disperazione e, soprattutto, per avermi sopportata. Adesso lo scrivo nero su bianco: sei il miglior relatore del mondo!

In secondo luogo ringrazio Catherine McCammon e Tiziana Boffa Ballaran, per aver vegliato sul mio operato durante la mia permanenza al BGI, per avermi insegnato molto in soli due mesi e per aver accolto con indulgenza anche i miei piccoli disastri in laboratorio!

Ringrazio Michael Carpenter, per la pazienza e la premura con le quali mi ha seguito durante la mia breve, ma intensa, parentesi anglosassone.

Grazie poi a Matteo Alvaro, che ha dedicato non poco del suo tempo ad educarmi sui precetti di EosFit e sul sacro calcolo delle "isomeke", a Donato Belmonte, che mi ha fornito i preziosi dati sull'espansione termica della coesite, e a Mauro Prencipe.

Ringrazio anche Luca Peruzzo, guru del SEM, e i maghi di laboratorio Hubert Schulze e Leonardo Tauro, senza i quali probabilmente non potrei vantarmi per il miglior campione policristallino per la RUS mai sintetizzato!

Un ringraziamento veramente sentito va ora a coloro i quali mi hanno generosamente offerto il loro supporto nel corso di questi mesi. Primo fra tutti Mattia che, essendo il connazionale più prossimo a me lungo gli interminabili corridoi del BGI, mi ha visto comparire implorante sulla soglia del suo ufficio più volte di quante mi fossero "concesse". Poi Esther, che da testimone involontaria si

è trasformata in complice in occasione dell'ormai famigerato "water event". Infine Sula, alla quale mi appoggio quando non trovo Fabrizio (o meglio, proprio per rintracciare Fabrizio!), e Luca che, insieme a Sula, mi ha elargito i viveri (letteralmente) e le nozioni di prima necessità al mio arrivo in Germania.

Terminata la parte più squisitamente scientifica, passiamo ora a quella affettivo-goliardica.

Il primo, gigantesco, ringraziamento va all'HAPG (Highly Alcoholic Paduan Geologists), associazione geologica di elevato spessore internazionale, che può vantare il più alto Impact Factor nel suo ambito di ricerca. DIN DON!

A seguire un caloroso grazie al NeedForSpritz, per gli immancabili appuntamenti rigeneranti del mercoledì e, perché no, anche degli altri giorni della settimana…

Grazie alla ConfrATTernita, un gruppo fin troppo segreto perché possa svelarne gli intenti su queste pagine.

Grazie ai Merluzzi Findus, perché insieme siamo entrati nel firmamento delle squadre di consolidata fama al Torneo di Volley dell'Ederle. È stato per me un vero onore capitanarvi per tre anni consecutivi!

Grazie all'Orda e al Club dei B., semplicemente perché viviamo in branco da quasi dieci anni, quindi il ringraziamento ci sta e basta.

Grazie infinite a Silvia, nonostante ci abbia tradito con la "Città che pur pei ratti par 'na fogna", ad Andrea, che mi ha portato dal lato oscuro della forza, e a Matteo, che malgrado tutto continua a farmi le sue "Sorprese" (OH MIO DIO!).

Un omaggio poi ai "Tre Scalini", al "Madrid", all'"Oktoberfest", ai "Navigli", all'"Ederle" e al "Tilly's Pub", luoghi di ristoro, ma, soprattutto, di perdizione.

Grazie al Sasso Guida, che mi ricorda sempre di non trasgredire.

Un ringraziamento va anche alla Biblioteca Civica di Tolmezzo, a cui probabilmente spetta gran parte del merito per avermi fatto concludere questa carriera accademica, nonostante l'odiatissima "Ora del racconto".

Infine grazie a mamma e papà, che probabilmente dopo questa sfilza di ringraziamenti crederanno di aver finanziato la mia adesione a sette di dubbia moralità, piuttosto che i miei studi.

Appendix A

Equations of State

An Equation of State (EoS) basically defines the variation of volume (or equivalently density) with pressure, and sometimes temperature, of a certain material.

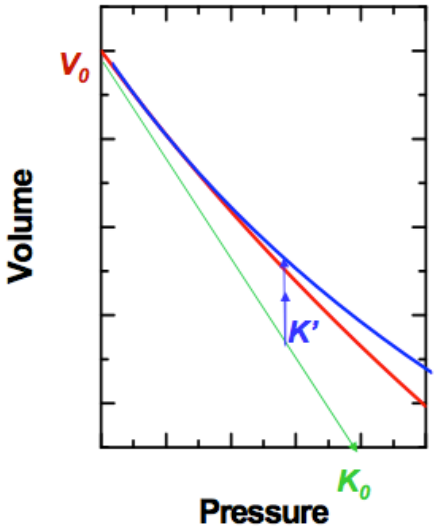

Fig. A.1: P-V diagram.

The variation of the volume of a solid with pressure is characterized by the bulk modulus, defined as $K = -V\,(\partial P/\partial V)$, that expresses the stiffness of the material. EoS are calculated in terms of the values of bulk modulus and its pressure derivatives, $K' = \partial K/\partial P$ and $K'' = \partial^2 K/\partial P^2$, evaluated at zero pressure, knowing a-priori the room pressure volume V_0 (Fig. A.1). All these parameters can be determined from *P-V* or *K-P* measurements. Diffraction experiments at high pressures provide measurement of the variation of the unit-cell parameters of the sample, and thereby the variation of its volume, with pressure. Once obtained a *P-V* diagram it is necessary to choose an EoS to fit the data, considering that there is no absolute thermodynamic basis for specifying the correct form of an EoS, and that the assumptions it is based on must be judged

only in terms of the accuracy with which it reproduces experimental data for volume or elasticity.

There are four main isothermal EoS:

a) Murnaghan. The Murnaghan EoS (Murnaghan, 1937) can be derived by assuming K is linear with P: $P_{VT} = \frac{K_{0T}}{K'_{0T}}\left[\left(\frac{V_{0T}}{V}\right)^{K'_{0T}} - 1\right]$. This EoS has a simple functional form, so it is often exploited for thermo databases, but it does not fit P-V data for $V/V_0 < 0.9$.

b) Tait. The "modified Tait equation" by Huang and Chow (1974) is a generalised form of the Murnaghan EoS which remains easily invertible: $P_{VT} = \frac{1}{b}\left(\left[\frac{(V_{PT}/V_{0T})+a-1}{a}\right]^{-1/c} - 1\right)$ and $V_{PT} = V_{0T}\left(1 - a(1 - (1 + bP)^{-c})\right)$. Because the Tait EoS is invertible, the expressions for the bulk modulus and its pressure derivatives as a function of pressure can be obtained directly by differentiation with respect to pressure of the expression for the volume: $K_{PT} = K_{0T}\left(\frac{V_{PT}}{V_{0T}}\right)(1 + bP)^{(c+1)}$.

c) Birch-Murnaghan. This is a "Finite strain EoS", derived (Birch, 1947) from the assumption that the strain energy of a solid undergoing compression can be expressed as a Taylor series in the finite strain, f. The Birch-Murnaghan EoS is based upon the Eulerian strain, $f_E = \left[(V_{0T}/V_{PT})^{2/3} - 1\right]/2$. Expansion to fourth order in the strain yields an EoS:

$$P = 3K_{0T}f_E(1 + 2f_E)^{\frac{5}{2}}\left(1 + \frac{3}{2}(K'_{0T} - 4)f_E + \frac{3}{2}\left(K_{0T}K''_{0T} + (K'_{0T} - 4)(K'_{0T} - 3) + \frac{35}{9}\right)f_E^2\right)$$

This EoS fits P-V data for V/V_0 to 0.8, therefore it is good for crust and mantle, and provides a correct K_{0T}, but cannot be easily inverted.

d) **Natural strain.** Poirier and Tarantola (1998) derived an EoS from an assumed relationship between free energy and strain and based upon the "natural" measure of linear strain, $f_N = 1/3\, ln(V_0/V)$. Expansion to fourth order in the strain yields an EoS:

$$P = 3K_{0T}\left(\frac{V_{0T}}{V_{PT}}\right) f_N \left[1 + \frac{3}{2}(K'_{0T} - 2)f_N + \frac{3}{2}(1 + K_{0T}K''_{0T} + (K'_{0T} - 2) + (K'_{0T} - 2)^2)f_N^2\right]$$

e) **Vinet.** Vinet et al. (1987) derived an EoS from general inter-atomic potential to represent the volume variation with pressure under very high compression:

$$P = K_{0T}\frac{3f_V}{(1-f_V)^2} exp\left(\frac{3}{2}(K'_{0T} - 1)f_V\right), \text{ where } f_V = 1 - \left(\frac{V_{PT}}{V_{0T}}\right)^{\frac{1}{3}}.$$

This EoS is not intended for materials with significant degrees of internal structure freedom, and does not allow a refinable *K''*.

To determine which truncation must be assumed, the *P*-*V* data are transformed into f_E and F_E and plotted with f_E as the abscissa (Fig. A.2).

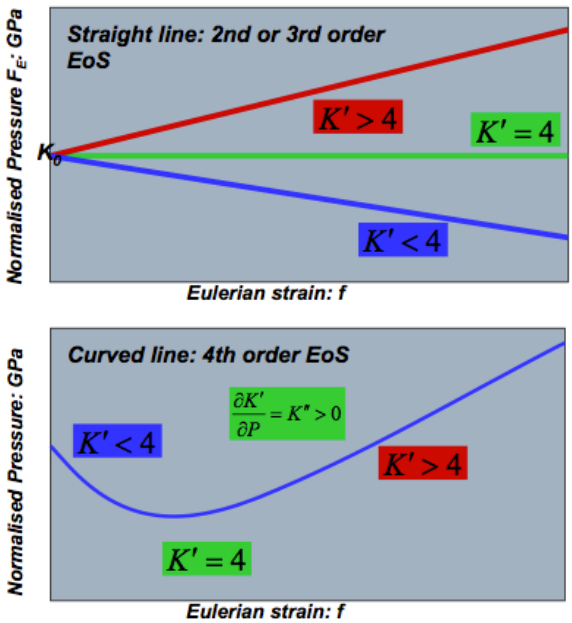

Fig. A.2: *f*-*F* plots.

Appendix B

Mathematical theory behind RUS

RUS is used to measure the normal frequencies of vibration of an object. First you have to solve the problem of calculating the natural frequencies in terms of sample dimensions, mass, and a set of hypothetical elastic constants (the **forward problem**). Then you have to apply a nonlinear inversion algorithm to find the elastic constants from the measured natural frequencies (the **inverse problem**).

B.I. Lagrangian minimization

All RUS measurements are performed on samples that are free vibrators. Because a complete analytical solution for the free vibrations of solids does not exist, one must rely on approximations. Finite-element methods base on balancing the forces on a differential volume element and calculating its response. Energy minimization methods, on the other hand, determine the minimum energy, and thus the equilibrium configuration for the object. Among the energy minimization techniques, the Lagrangian minimization is the most used in the RUS analyses because of its advantage in speed (an order of magnitude smaller than the finite-element methods).

The procedure begins with an object of volume *V*, bounded by its free surface *S*. The Lagrangian is given by

$$L = \int_V (KE - PE) dV \tag{B.1}$$

where KE is the kinetic energy density

$$KE = \frac{1}{2} \sum_i \rho \omega^2 u_i^2 \tag{B.2}$$

and PE is the potential energy density

$$PE = \frac{1}{2} \sum_{i,j,k,l} c_{ijkl} \frac{du_i}{dx_j} \frac{du_k}{dx_l} \tag{B.3}$$

Here, u_i is the i^{th} component of the displacement vector, ω is the angular frequency from harmonic time dependence, c_{ijkl} is a component of the elastic tensor, and ρ is the density. Subscripts i, j, etc., refer to Cartesian coordinate directions.

To find the minimum of the Lagrangian, you must calculate the differential of L as a function of u, the arbitrary variation of u in V and on S. This gives eq. (B.4):

$$\delta L = \int_V \left\{ \sum_i \left[\rho\omega^2 u_i - \sum_{j,k,l} c_{ijkl} \frac{\partial^2 u_k}{\partial x_j \partial x_l} \right] \delta u_i \right\} dV - \int_S \left\{ \sum_i \left[\sum_{j,k,l} \vec{n_j} c_{ijkl} \frac{\partial u_k}{\partial x_l} \right] du_i \right\} dS$$

Because u_i is arbitrary in V and on S, both terms in square brackets must be zero. Setting the first term equal to zero yields the elastic wave equation. The second square bracketed term is an expression of free-surface boundary conditions; $\vec{n_j}$ is the unit vector normal to S. For a free body (as we assume it), the latter term sums to zero and can be ignored.

Thus the set of u_i that satisfies the previously mentioned conditions are those displacements that correspond to ω being a normal-mode frequency of the system. This suggests that the normal vibrations of an object (Fig. B.1) may be calculated by applying a variational method (in our case the Rayleigh-Ritz variational method, explained in the next paragraph) to determine both the normal mode frequencies and the description of the physical oscillations. To quote Visscher, getting both equations from the basic

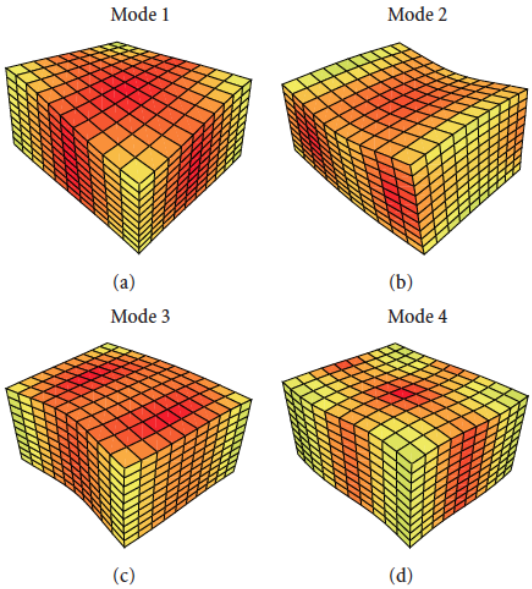

Fig. B.1: Computer-generated illustrations of some normal modes of vibrations for a rectangular parallelepiped sample (from Li and Gladden, 2010).

Lagrangian is “a mathematical fortuity that may have occurred during a lapse in Murphy’s vigilance”.

B.II. Rayleigh-Ritz Variational Method

The actuation of this approach requires the expansion of the u_i in a set of basis functions appropriate to the geometry of the body, substituting that expression into Eq. (B.1) and reducing the problem to that of diagonalizing a N×N matrix (eigenvalue problem). The stationary points of the Lagrangian are found by solving the eigenvalue problem resulting from Eq. (B.4), that is,

$$\omega^2 E a = \Gamma a \tag{B.5}$$

where a are the approximations to the motion expanded in a complete basis set, E comes from the kinetic energy term, and Γ comes from the elastic energy term.

The order of the matrices is ~103 for good approximations. Equation (B.5) determines the resonance frequencies from the elastic moduli.

B.III. The Inverse Problem

The inverse problem of deducing the elastic constants from a measured spectrum of mechanical resonances has no analytical solution, so it needs to be solved by computational methods. For the indirect method, a starting resonant frequency spectrum, f_n^{cal} (n=1,2,...) is calculated using estimated values for the elastic constants and the known sample dimensions and density. The difference between the calculated and measured resonance frequency spectrum, f_n^{mea} (n=1,2,...) is quantified by a Figure-of-merit function,

$$F = \sum_n w_n \ (f_n^{cal} - f_n^{mea})^2 \tag{B.6}$$

where w_n (n=1,2,...) are weight coefficients reflecting the confidence on individual resonance measurements. Then, a minimization of the function F is sought by regressing the values of all the elastic constants using computer software developed for this process.

Appendix C

Text to be inserted in the Igor Pro Procedure Window, which creates the 'lorentz2' curve fitting function, for fitting resonance peaks with an asymmetric Lorentzian profile.

```
function lorentz2 (w,x) : FitFunc
wave w
variable x
variable AoverB = w[2]/w[3]
variable B2 = w[4]/AoverB
return x < w[1] ? w[0]+w[5]*x+w[2]/((x-w[1])^2+w[3]) :
 w[0]+w[5]*x+w[4]/((x-w[1])^2+B2)
end

function halfwidth (w,x)
wave w
variable x
variable AoverB=w[2]/w[3]
variable B2 = w[4]/AoverB
return sqrt(B2)+sqrt(w[3])
end
```

This text, written by Dr. Richard Harrison (University of Cambridge), describes the asymmetric Lorentzian peak shape using equation 9.2. It includes the conditions that two different profiles should be fit on either side of the peak maximum, but that the baseline, the value of f_0 and the ratio A/B must be kept constant for both sides of the resonance peak.

Appendix D

Calculation performed to infer the shear modulus (G) of coesite from the adiabatic bulk modulus (K_s) reported by Angel et al. (2001).

Considering that:

- $V_P = \sqrt{\frac{K_S + \frac{4}{3}G}{\rho}}$ is the velocity of longitudinal (or compressional) waves;
- $V_s = \sqrt{\frac{G}{\rho}}$ is the velocity of transverse (or shear) waves;
- The V_P/V_S ratio, constant for any material, in the case of coesite is typically $1.75 - 1.77$ (Hacker and Abers, 2012).

$$V_s \cdot 1.76 = \sqrt{\frac{K_S + \frac{4}{3}G}{\rho}}$$

$$V_s = \frac{1}{1.76}\sqrt{\frac{K_S + \frac{4}{3}G}{\rho}}$$

$$\left(\sqrt{\frac{G}{\rho}}\right) = \left(\frac{1}{1.76}\sqrt{\frac{K_S + \frac{4}{3}G}{\rho}}\right)$$

$$G = 0.3228\left(K_S + \frac{4}{3}G\right)$$

$$G = 0.3228\,K_S + 0.4304\,G$$

$$G - 0.4304\,G = 0.3228\,K_S$$

$$0.5696\,G = 0.3228\,K_S$$

$$\boxed{G = 0.5667\,K_S}$$